



## DIPLOMARBEIT

# Characterization of the Nonlinear Light Emission by the Liquid Scintillator Used in the Daya Bay Experiment

Ausgeführt an der  
**Technischen Universität Wien**

unter Anleitung von  
Univ.Prof. Dipl.-Ing. Dr.techn. Gerald BADUREK

in Zusammenarbeit mit dem

**Lawrence Berkeley National Laboratory**

unter Anleitung von  
Prof. Herbert STEINER  
und  
Dr. Daniel DWYER

durch

Christian DORFER  
Patergassen 63  
9564 Reichenau

---

Ort, Datum

---

Unterschrift



# Abstract

This thesis has been prepared within the Daya Bay group at the Lawrence Berkeley National Laboratory in California. It describes the measurement of the nonlinearity in light emission by a linear alkylbenzene-based liquid scintillator in response to electrons with kinetic energies from  $\sim 0.2$  to  $\sim 1.0$  MeV. The electrons were generated inside the liquid scintillator volume via Compton scattering of 1.332 MeV gamma rays emitted by a 2.59 MBq  $^{60}\text{Co}$  radioactive source. A Compton spectrometer was designed and custom-built to scan over the full range of electron energies. Geant4-based simulations were used to optimize the spectrometer design and estimate systematic effects from energy loss and multiple scattering. The ratio of light emitted relative to the electron's kinetic energy was found to be  $(17.59 \pm 1.24)$  % lower at 0.2 MeV compared to 1.0 MeV, demonstrating significant nonlinearity. This precision determination of scintillator nonlinearity will facilitate the improved measurement of reactor antineutrino oscillation by the Daya Bay experiment.

# Kurzfassung

Diese Forschung für diese Arbeit wurde in der Daya Bay Gruppe des Lawrence Berkeley National Laboratory in Kalifornien durchgeführt. Die Arbeit beschreibt die Messung der nichtlinearen Lichtemission von auf flüssigem Alkylbenzol-basierten Szintillator bei Anregung durch energetische Elektronen zwischen  $\sim 0.2$  und  $\sim 1$  MeV. Die Elektronen wurden mit Hilfe von Compton-Streuung im Szintillatorvolumen erzeugt. Die Gamma-Strahlen dazu kamen von einer 2.59 MBq  $^{60}\text{Co}$  Quelle. Um den gesamten Energiebereich zu messen wurde ein Compton Spektrometer gebaut, welches mit Geant4-basierten Simulationen optimiert wurde. Geant4 wurde auch verwendet um systematische Fehler wie Vielfachstreuung innerhalb des Szintillators oder Energieverlust außerhalb des Szintillators abzuschätzen. Das gemessene Verhältnis von emittierten Licht in Abhängigkeit der Elektronenenergie betrug  $(17.59 \pm 1.24) \%$  für Elektronen zwischen 0.2 MeV und 1 MeV. Das Ergebnis wird helfen die Messungen von Neutrinooszillationen im Daya Bay Experiment zu verbessern.

# Acknowledgments

This thesis would not exist without my host, Professor Herbert Steiner, who made it possible for me to come to Lawrence Berkeley National Laboratory, invited me to stay at his place during my house hunting, provided me with tons of camping gear, and supported me wherever he could. I would also like to thank my supervisor, Professor Gerald Badurek at the Technical University of Vienna, who supported my endeavor to write my Master's thesis abroad, and who took care of all of the organizational tasks back home. At this point I would also like to thank all of my financial supporters, namely the Marshall Plan Foundation, the Erich Lackner Stiftung, students4excellence (now e-fellows.net), and Lawrence Berkeley National Laboratory, who covered all the costs of my stay in California.

Secondly, I would like to express my gratitude to the members of the Daya Bay group at Berkeley for all of their help and constructive input. First and foremost, I would like to thank Daniel Dwyer for his guidance and trust throughout the whole experiment. I have not yet worked with many people who have such a comprehensive knowledge of physics, data analysis, and programming, and who actually have the patience and skill to pass it on. I have also particularly benefited from discussions with Herbert Steiner and Kam-Biu Luk. Herb and Dan have both additionally been extremely helpful in providing feedback on everything that is written up in this thesis. I would further like to thank Cory W. Lee, who allowed me to use the machine shop he oversaw, helping me wherever he could.

Finally, my special thanks go to all the great people I got to know in Berkeley, as well as my family and friends back in Austria. I am especially grateful to my colleague at LBNL, Matt Kramer, for lending me his motorcycle so that I could get my driver's license in California. I would also like to mention the Cal Sailing Club, where I spent most of my free time during the summer and not only learned how to windsurf at a high level, but also met tons of interesting people.

# Contents

<b>1</b>	<b>Theoretical Background</b>	<b>1</b>
1.1	Overview of Neutrino Physics . . . . .	1
1.1.1	Neutrinos in Particle Physics . . . . .	1
1.1.2	Neutrino Oscillations . . . . .	2
1.1.3	Latest Results on Neutrino Oscillation Parameters . . . . .	5
1.1.4	Experiments . . . . .	6
1.2	Neutrino Detection with Organic Scintillators . . . . .	7
1.2.1	Principle of Detection . . . . .	7
1.2.2	Process of Light Generation . . . . .	8
1.2.3	Quenching . . . . .	10
1.3	Daya Bay Experiment . . . . .	11
1.3.1	Neutrino Detection Medium . . . . .	12
1.3.2	Detector Design . . . . .	13
1.3.3	Data Analysis . . . . .	15
<b>2</b>	<b>Experimental Method</b>	<b>19</b>
2.1	Compton Spectrometer . . . . .	20
2.1.1	Collimators and Source Handling . . . . .	21
2.1.2	Target Cell and Photomultiplier Tube Coupling . . . . .	25
2.2	Electronics . . . . .	27
2.2.1	Block Diagram and Trigger Description . . . . .	27
2.2.2	Detectors . . . . .	29
2.2.3	NIM System . . . . .	30
2.2.4	VME System . . . . .	30
2.3	Data Acquisition Software . . . . .	31
<b>3</b>	<b>Data Analysis</b>	<b>33</b>
3.1	Acquired Data . . . . .	33
3.2	Data Processing . . . . .	33
3.2.1	HPGe Detector Stability . . . . .	33
3.2.2	HPGe Detector Calibration . . . . .	34
3.2.3	PMT Charge Integration . . . . .	38
3.2.4	PMT Gain Stability . . . . .	40
3.3	Nonlinearity Analysis . . . . .	42
3.4	Error Propagation . . . . .	44
<b>4</b>	<b>Error Budget</b>	<b>45</b>
4.1	Gamma Energy Loss . . . . .	46
4.2	Accuracy of PMT Calibration . . . . .	46
4.3	Nonlinearity of the PMT System . . . . .	46
4.4	Bias of Fitting Procedure . . . . .	47
4.5	Other Effects . . . . .	49
<b>5</b>	<b>Summary and Results</b>	<b>50</b>
	<b>References</b>	<b>52</b>

# 1 Theoretical Background

## 1.1 Overview of Neutrino Physics

The first experiment that ever detected a neutrino was conducted in 1956 by Clyde L. Cowan and Frederick Reines[8]. In their experiment they used the inverse beta-decay reaction  $\bar{\nu}_e + p = n + e^+$  in a cadmium chloride solution to detect electron anti-neutrinos coming from a nuclear reactor. The detection principle of the experiment was to look for two  $\gamma$ -ray signals, one coming from the annihilation of the positron and the other one coming from the neutron's capture on a cadmium nucleus.

Frederick Reines was honoured with the 1995 Nobel Prize for this discovery. However the first prediction of neutrinos had been made 26 years earlier by Wolfgang Pauli, who proposed the particle in his famous letter to the Tübingen convention on radioactivity[19]. It was then Fermi, who later renamed Pauli's neutron to the neutrino, who provided the first theory to successfully explain the energy spectrum of beta decay, based on his 4-point beta decay Lagrangian, published in 1934.

In 1962, Leon Lederman, Melvin Schwartz, and Jack Steinberger detected the muon neutrino by utilizing an accelerator to produce muons and muon neutrinos[11]. The produced particles were sent through thick steel plates that only allowed the muon neutrinos to pass. A spark chamber, which was located behind the steel plates, detected interactions of the muon neutrino.

Another milestone in experimental neutrino physics was the Homestake experiment of John Bahcall and Raymond Davis, Jr. in 1964[12]. The experiment measured the flux of electron anti-neutrinos coming from the sun. Bahcall's calculations predicted an event rate of 2-7 per day, but the experiment only measured 1, leading to the so called solar neutrino problem[17]. The experiment was the first indication of the validity of a prediction made by Bruno Pontecorvo, Ziro Maki, Masami Nakagawa, and Shoichi Sakata in 1956 [21]. They proposed that neutrinos are not massless, and thus oscillate between flavors as they propagate.

The scientific community was skeptical about these statements, but many experiments that have followed the Homestake experiment, including Kamiokande, Super-Kamiokande, GALLEX, Borexino, KamLand, and others, confirmed these models. Davis and Masatoshi Koshiba (the leading scientist of the Kamiokande and Super-Kamiokande experiments) were both awarded the Nobel Prize for their work in 2002.

The tau neutrino's existence was implied by an experiment performed by Martin Lewis Perl and his colleagues at SLAC, before it was finally found in the DONUT experiment at Fermilab in 2000[23][18]. The detector of the DONUT experiment used emulsion plates to detect  $\tau$  neutrinos. The signature of a  $\tau$  event was the sudden appearance of multiple tracks in the detector, with one of these tracks having a 'kink' that resulted from the decay of a  $\tau$ -lepton.

All the observations mentioned have led to many experiments all around the world that were, are, or will be carried out to precisely measure the parameters describing the neutrino's behavior. A small selection of these experiments will be described in section 1.1.4.

### 1.1.1 Neutrinos in Particle Physics

In his 1930 letter[19], Pauli describes the neutrino as a weakly interacting spin-1/2 particle, which travels at less than the speed of light, and has a mass of the order of the electron mass, but certainly not bigger than 1 % of the proton mass. When the Standard Model (SM) of particle physics was formulated in the 1960s by Abdus Salam[24], Sheldon Glashow[14] and Steven Weinberg[27], neutrinos were included as massless spin-1/2 fermions that form 3 families of lepton isospin doublets (figure 1). These doublets are formed by neutrinos and their massive electrically charged partners: the electron ( $e^-$ ), muon ( $\mu^-$ ), and tau ( $\tau^-$ ), from which they also inherit their names: the electron neutrino ( $\nu_e$ ), muon neutrino ( $\nu_\mu$ ), and tau neutrino ( $\nu_\tau$ ).

Since neutrinos are massless in the SM, their chirality is equivalent to their helicity, and only left-handed neutrinos should and have been observed up to this point. Neutrinos only interact weakly in charged (CC) or neutral current (NC) interactions. The propagators of these interactions are the  $W^\pm$  boson for CC and the  $Z^0$  boson for NC interactions. CC interactions are the relevant ones for the Daya Bay experiment, where the electron antineutrinos are detected in inverse beta decay reactions.

Starting with the Homestake experiment, it has been proven multiple times that neutrino oscillations occur[10]. Consequently, neutrinos must have a non-zero mass, which is contrary to the assumption used in the SM. Many theories on how neutrinos obtain mass have been formulated, but no experiment has yet been able to determine the correct one.

Three generations  
of matter (fermions)

	I	II	III	
mass →	2.4 MeV/c <sup>2</sup>	1.27 GeV/c <sup>2</sup>	171.2 GeV/c <sup>2</sup>	0
charge →	$\frac{2}{3}$	$\frac{2}{3}$	$\frac{2}{3}$	0
spin →	$\frac{1}{2}$	$\frac{1}{2}$	$\frac{1}{2}$	1
name →	<b>u</b> up	<b>c</b> charm	<b>t</b> top	<b>γ</b> photon
Quarks	4.8 MeV/c <sup>2</sup>	104 MeV/c <sup>2</sup>	4.2 GeV/c <sup>2</sup>	0
	$-\frac{1}{3}$	$-\frac{1}{3}$	$-\frac{1}{3}$	0
	$\frac{1}{2}$	$\frac{1}{2}$	$\frac{1}{2}$	1
	<b>d</b> down	<b>s</b> strange	<b>b</b> bottom	<b>g</b> gluon
Leptons	<2.2 eV/c <sup>2</sup>	<0.17 MeV/c <sup>2</sup>	<15.5 MeV/c <sup>2</sup>	91.2 GeV/c <sup>2</sup>
	0	0	0	0
	$\frac{1}{2}$	$\frac{1}{2}$	$\frac{1}{2}$	1
	<b>ν<sub>e</sub></b> electron neutrino	<b>ν<sub>μ</sub></b> muon neutrino	<b>ν<sub>τ</sub></b> tau neutrino	<b>Z<sup>0</sup></b> Z boson
Gauge bosons	0.511 MeV/c <sup>2</sup>	105.7 MeV/c <sup>2</sup>	1.777 GeV/c <sup>2</sup>	80.4 GeV/c <sup>2</sup>
	-1	-1	-1	±1
	$\frac{1}{2}$	$\frac{1}{2}$	$\frac{1}{2}$	1
	<b>e</b> electron	<b>μ</b> muon	<b>τ</b> tau	<b>W<sup>±</sup></b> W boson

Figure 1: Fundamental particles in the Standard Model: The force carrying bosons in red and the three generations of matter represented as leptons (green) and quarks (purple).

### 1.1.2 Neutrino Oscillations

In the first days of neutrino physics, the theory of neutrino oscillations formulated in 1956 by Pontecorvo, Maki, Nakagawa, and Sakata[21] was viewed with great skepticism, until later experiments proved its validity. The foundation of the neutrino oscillation theory is that flavor states ( $\nu_e, \nu_\mu, \nu_\tau$ ) are rotated with respect to the mass states ( $\nu_1, \nu_2, \nu_3$ ). While neutrinos can only be created and detected in their flavor eigenstates, their superposition of mass eigenstates varies as they propagate. The phase differences between the mass eigenstates cause the neutrino's flavor composition to change in transit. The matrix that describes this mixing is the 3x3 Pontecorvo-Maki-Nakagawa-Sakata (PMNS) matrix:

$$\begin{pmatrix} \nu_e \\ \nu_\mu \\ \nu_\tau \end{pmatrix} = \begin{pmatrix} 1 & 0 & 0 \\ 0 & c_{23} & s_{23} \\ 0 & -s_{23} & c_{23} \end{pmatrix} \begin{pmatrix} c_{13} & 0 & s_{13}e^{-i\delta_{CP}} \\ 0 & 1 & 0 \\ -s_{13}e^{i\delta_{CP}} & 0 & c_{13} \end{pmatrix} \begin{pmatrix} c_{12} & s_{12} & 0 \\ -s_{12} & c_{12} & 0 \\ 0 & 0 & 1 \end{pmatrix} \begin{pmatrix} 1 & 0 & 0 \\ 0 & e^{i\alpha_1/2} & 0 \\ 0 & 0 & e^{i\alpha_2/2} \end{pmatrix} \begin{pmatrix} \nu_1 \\ \nu_2 \\ \nu_3 \end{pmatrix} \quad (1)$$

$c_{ij} = \cos(\theta_{ij})$ ,  $s_{ij} = \sin(\theta_{ij})$ ,  $\theta_{ij}$  are the mixing angles and  $\delta_{CP}$  is the CP-violating phase. The Majorana phases  $\alpha_1$  and  $\alpha_2$  in the last matrix describe the rate of neutrinoless double  $\beta$ -decay. If  $\delta_{CP}$  is non-zero, CP-symmetry is violated.

Compared to its analogue in quantum chromodynamics, the Cabibbo-Kobayashi-Maskawa (CKM) matrix, the PMNS matrix behaves completely differently. Instead of having diagonal elements close to 1 and off-diagonal elements close to zero, as in the CKM matrix, the PMNS matrix has large off-diagonal values comparable to its diagonal elements. Due to these off-diagonal elements, more than one mass eigenstate contributes significantly each flavor eigenstate.

The mixing angles as we know them today were obtained from different types of experiments:  $\theta_{23}$  of the first matrix was obtained through atmospheric experiments,  $\theta_{13}$  through reactor neutrino experiments, and  $\theta_{12}$  through solar experiments and more recently through KamLAND, a long-baseline reactor neutrino experiment. Often, the three-flavor mixing is simplified to a two-flavor model. As we will see later in this section, among the mass eigenstates there are two widely separated scales of mass-squared splittings (which govern the oscillation frequencies), so that this approximation is often accurate enough. With  $\hbar = c = 1$ , the mixing between flavor and mass eigenstates in vacuum can be expressed as:

$$|\nu_\alpha\rangle = \sum_i U_{\alpha i} |\nu_i\rangle \quad (2)$$

Where  $\alpha$  denotes the flavor and  $i$  the mass eigenstates. The time evolution of a mass eigenstate is given by:

$$|\nu_i(t)\rangle = e^{-iE_i t} |\nu_i\rangle \quad (3)$$

Since neutrino masses are estimated to be less than a few eV, and the observed energies are on the order of MeV, the following approximation for  $E_i$  is valid:

$$E_i = \sqrt{p^2 + m_i^2} \simeq p + \frac{m_i^2}{2p} \simeq E + \frac{m_i^2}{2E} \quad (4)$$

The unitary 2x2 transformation matrix that describes the mixing of flavor and mass states in the 2-particle case can then be written as:

$$\begin{pmatrix} \nu_\alpha \\ \nu_\beta \end{pmatrix} = \begin{pmatrix} \cos(\theta) & \sin(\theta) \\ -\sin(\theta) & \cos(\theta) \end{pmatrix} \begin{pmatrix} \nu_1 \\ \nu_2 \end{pmatrix} \quad (5)$$

With equation (5) and (3), the time evolution of a neutrino created in a flavor state  $\alpha$  is then:

$$|\nu_\alpha(t)\rangle = e^{-iE_1 t} \cos(\theta) |\nu_1\rangle + e^{-iE_2 t} \sin(\theta) |\nu_2\rangle \quad (6)$$

From equation (6), the survival probability for flavor  $\alpha$  after a certain distance can be expressed as:

$$P_{\nu_\alpha \rightarrow \nu_\alpha} = |\langle \nu_\alpha | \nu_\alpha(t) \rangle|^2 = 1 - \sin^2(2\theta) \sin^2\left(\frac{\Delta m^2 L}{4E}\right) \quad (7)$$

The time in equation (6) was replaced by distance through the relation  $L \simeq c \cdot t$ . The mixing angle in the first sine of equation (7) determines the amplitude of the oscillation, while the squared mass difference in the second term  $\Delta m_{21}^2 = m_2^2 - m_1^2$  determines the frequency of oscillation. Equation (7) written in SI units gives:

$$P_{\nu_\alpha \rightarrow \nu_\alpha} = |\langle \nu_\alpha | \nu_\alpha(t) \rangle|^2 = 1 - \sin^2(2\theta) \sin^2\left(1.267 \frac{\Delta m^2 L}{E} \frac{\text{GeV}}{\text{eV}^2 \text{km}}\right) \quad (8)$$

Here we can clearly see why using the two-flavor simplification instead of the cumbersome three-flavor theory is adequate: Big differences in oscillation frequency (due to different mass splittings) and amplitudes (due to different mixing angles) cause equation (8) to behave very differently for different flavors. For completeness, an equation describing the survival probability of an electron

neutrino, considering all three flavors and excluding any CP-violating phase, is given in (9) where  $\theta_{ij} = 1.267 \frac{L \Delta m_{ij}^2}{E}$ :

$$P_{\nu_e \rightarrow \nu_e} = 1 - \cos^4(\theta_{13}) \sin^2(\theta_{12}) \sin^2(\Delta m_{21}) - \sin^2(\theta_{13}) \left( \cos^2(\theta_{12}) \sin^2(\Delta m_{31}) + \sin^2(\theta_{12}) \sin^2(\Delta m_{32}) \right) \quad (9)$$

One thing to note at this point is the representation Daya Bay chooses for the squared mass differences: Since  $\cos^2(\theta_{12}) \sim 0.7$  and  $\sin^2(\theta_{12}) \sim 0.3$  the second term of equation (9) is abbreviated as  $\sin^2(\Delta m_{ee})$  leading to a new representation, which is independent of the mass hierarchy (discussed later) and easier to fit:

$$P_{\nu_e \rightarrow \nu_e} = 1 - \cos^4(\theta_{13}) \sin^2(\theta_{12}) \sin^2(\Delta m_{21}) - \sin^2(\theta_{13}) \sin^2(\Delta m_{ee}) \quad (10)$$

Figure 2 shows the survival probability of a 4 MeV neutrino over the distance obtained from equation (10) with oscillation parameters from the next chapter.

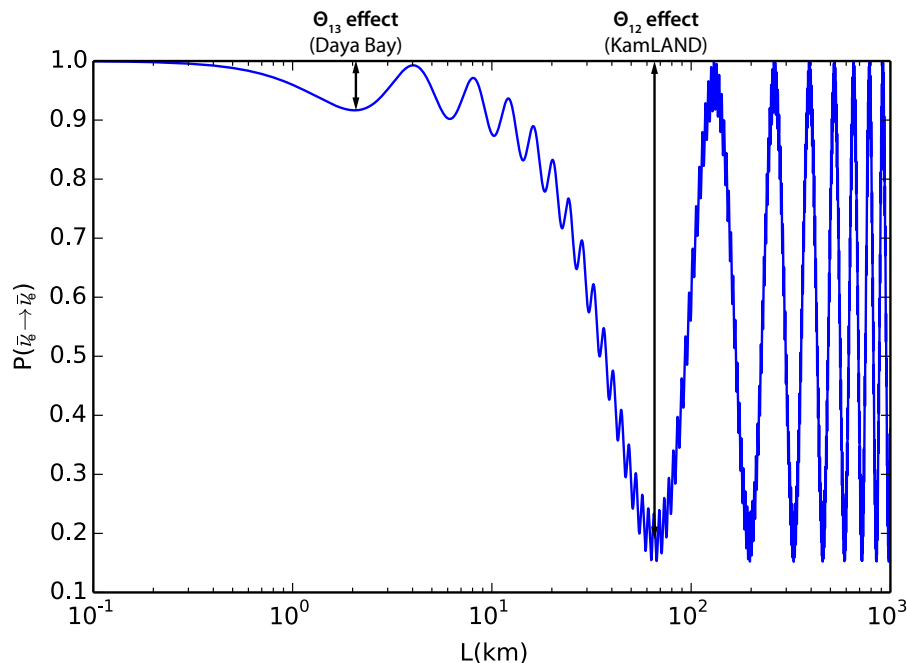


Figure 2: Survival probability for a 4 MeV electron (anti-) neutrino in vacuum as a function of distance from of its origin.

The plot shows the two superimposed oscillations very clearly. It also shows that the survival probability has its first minimum at a distance of around 2 km. This is chosen as the distance between reactor and far detector for reactor-based  $\theta_{13}$  neutrino oscillations experiments.

The discussion above was based on vacuum neutrino oscillations. In the case of neutrinos penetrating matter, the Mikheyev-Smirnov-Wolfenstein (MSW) effect has to be considered. It describes changes in the neutrino mass eigenstates through coherent forward scattering of electron neutrinos on electrons as they travel through matter. The scattering leads to a different effective mass of the electron neutrino and therefore different time evolution of mass eigenstates. The effect is negligible for short baselines like the one used in the Daya Bay experiment, but it is

significant for solar neutrino experiments where neutrinos travel from the core of the sun to the surface before leaving the sun.

### 1.1.3 Latest Results on Neutrino Oscillation Parameters

Seven parameters describe neutrino mixing: The three mixing angles ( $\theta_{23}$ ,  $\theta_{13}$ ,  $\theta_{12}$ ), the squared mass differences ( $\Delta m_{23}^2$ ,  $\Delta m_{13}^2$ ,  $\Delta m_{21}^2$ ), and the CP-violating phase ( $\delta_{CP}$ ). The current status[15] of these parameters is shown in figure 4, which distinguishes between the two different ways neutrino mass states can be arranged. In general, all masses are related through  $\Delta m_{13}^2 = \Delta m_{21}^2 + \Delta m_{23}^2$  (where  $\Delta m_{21}^2$  is positive by convention), but unfortunately the sign of  $\Delta m_{23}^2$  is not known, leading to two possibilities for the ordering of the masses, as shown in figure<sup>1</sup> 3.

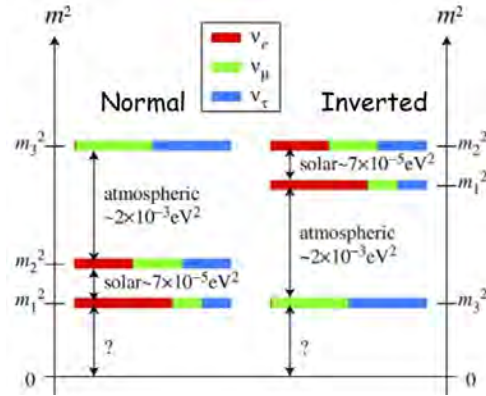


Figure 3: Mass hierarchy

In the normal hierarchy case,  $m_3$  is the heaviest mass state, while in the inverted hierarchy it is the lightest one. Figure 3 points out the possibility that the lightest mass state could be zero, however this is considered unlikely.

	Normal Ordering ( $\Delta\chi^2 = 0.97$ )		Inverted Ordering (best fit)		Any Ordering
	bfp $\pm 1\sigma$	$3\sigma$ range	bfp $\pm 1\sigma$	$3\sigma$ range	$3\sigma$ range
$\sin^2 \theta_{12}$	$0.304^{+0.013}_{-0.012}$	$0.270 \rightarrow 0.344$	$0.304^{+0.013}_{-0.012}$	$0.270 \rightarrow 0.344$	$0.270 \rightarrow 0.344$
$\theta_{12}/^\circ$	$33.48^{+0.78}_{-0.75}$	$31.29 \rightarrow 35.91$	$33.48^{+0.78}_{-0.75}$	$31.29 \rightarrow 35.91$	$31.29 \rightarrow 35.91$
$\sin^2 \theta_{23}$	$0.452^{+0.052}_{-0.028}$	$0.382 \rightarrow 0.643$	$0.579^{+0.025}_{-0.037}$	$0.389 \rightarrow 0.644$	$0.385 \rightarrow 0.644$
$\theta_{23}/^\circ$	$42.3^{+3.0}_{-1.6}$	$38.2 \rightarrow 53.3$	$49.5^{+1.5}_{-2.2}$	$38.6 \rightarrow 53.3$	$38.3 \rightarrow 53.3$
$\sin^2 \theta_{13}$	$0.0218^{+0.0010}_{-0.0010}$	$0.0186 \rightarrow 0.0250$	$0.0219^{+0.0011}_{-0.0010}$	$0.0188 \rightarrow 0.0251$	$0.0188 \rightarrow 0.0251$
$\theta_{13}/^\circ$	$8.50^{+0.20}_{-0.21}$	$7.85 \rightarrow 9.10$	$8.51^{+0.20}_{-0.21}$	$7.87 \rightarrow 9.11$	$7.87 \rightarrow 9.11$
$\delta_{CP}/^\circ$	$306^{+39}_{-70}$	$0 \rightarrow 360$	$254^{+63}_{-62}$	$0 \rightarrow 360$	$0 \rightarrow 360$
$\frac{\Delta m_{21}^2}{10^{-5} \text{ eV}^2}$	$7.50^{+0.19}_{-0.17}$	$7.02 \rightarrow 8.09$	$7.50^{+0.19}_{-0.17}$	$7.02 \rightarrow 8.09$	$7.02 \rightarrow 8.09$
$\frac{\Delta m_{3\ell}^2}{10^{-3} \text{ eV}^2}$	$+2.457^{+0.047}_{-0.047}$	$+2.317 \rightarrow +2.607$	$-2.449^{+0.048}_{-0.047}$	$-2.590 \rightarrow -2.307$	$[+2.325 \rightarrow +2.599]$ $[-2.590 \rightarrow -2.307]$

Figure 4: Current knowledge of neutrino oscillation parameters

<sup>1</sup><https://inspirehep.net/record/1209723/files/mass.png>

Nothing is known about how neutrinos obtain mass, but many theories have been proposed. One of them is called the seesaw mechanism, where each neutrino has a very heavy, not-yet-observed partner. In the seesaw theory, the light neutrinos (the ones that are currently observed in experiments) have almost zero mass and therefore no Higgs couplings, while the heavy ones have a mass at some symmetry breaking scale. The heavier the heavy partner gets, the lighter the lighter one is, hence the name seesaw effect. Some superposition of the light and heavy particle fields in the seesaw theory could then lead to the neutrino masses we know today.

#### 1.1.4 Experiments

Neutrino experiments can be separated into solar, atmospheric, accelerator, decay, and reactor based experiments. Different types of experiments focus on different parameters; for example,  $\theta_{12}$  was mainly determined in solar neutrino experiments but has also been measured in the reactor based KamLAND experiment using a 180 km baseline. Determining  $\theta_{13}$  requires smaller baselines on the order of 1 - 4 kilometers for 1 - 10 MeV neutrinos. For disappearance experiments like Daya Bay, the length of the baseline is always selected to minimize the survival probability of a neutrino at the far detector, and therefore depends on neutrino energy and mass splitting.

The first experiments in neutrino physics were the Cowan-Reines experiment and the Homestake experiment, followed by Kamiokande, SAGE and Gallex. A very small subset of the many currently running and future experiments include:

- Object:  $m_\nu$

**KATRIN:** The Karlsruhe Tritium Neutrino Experiment aims to measure the mass of the electron anti-neutrino with sub-eV precision by examining the tail of the tritium beta spectrum. The complete system integration is planned for 2014.

**Project 8:** Like the KATRIN experiment, Project 8 measures the energies of electrons coming from tritium decay. However, the approach is different: The decay electrons are collected and trapped in magnetic fields where their cyclotron frequency is measured, from which their mass can be calculated. The difference between the measured electron mass and the 'true' electron mass equals the mass of the electron anti-neutrino. This experiment is meant to be very precise and is currently undergoing its first test phase.

- Object:  $\nu_\mu \rightarrow \nu_e$  oscillations

**T2K:** This accelerator-based muon experiment uses the J-PARC facility to generate a beam of muon neutrinos directed toward the Super-Kamiokande detector 295 km away. The aim of the experiment is to measure the oscillation of muon neutrinos to electron neutrinos, giving  $\theta_{13}$ . In 2013, the T2K collaboration announced that they have observed  $\nu_\mu$  to  $\nu_e$  oscillations[28].

- Object: Mass hierarchy and  $\delta_{CP}$

**LBNF:** The Long Baseline Neutrino Facility is a proposed long baseline neutrino experiment at Fermilab. The start of operation is planned to be in 2022.

**JUNO:** The Jiangmen Underground Neutrino Observatory (JUNO) uses a 20 kT detector to detect electron anti-neutrinos coming from the Yangjiang and Taishan nuclear power plants in China. The construction started in 2014 and is planned to be completed in 2019.

- Object:  $\theta_{13}$

Aside from **Daya Bay**, currently operating reactor-based experiments that also aim to determine  $\theta_{13}$  are **RENO** (Reactor Experiment for Neutrino Oscillations) in South Korea and **Double Chooz** at the Chooz Nuclear Power Plant in France. In 2012 RENO reported a  $4.9\sigma$  measurement of  $\theta_{13}$  being non-zero[3]. RENO's latest results[13] report a fit value of  $\sin^2(2\theta_{13}) = 0.101 \pm 0.008(stat.) \pm 0.010(syst.)$ . In July 2014, Double Chooz reported a background-subtracted measurement of  $\sin^2(2\theta_{13}) = 0.102 \pm 0.028(stat.) \pm 0.033(syst.)$ [2]. This result was later corrected to  $\sin^2(2\theta_{13}) = 0.09 \pm 0.03$ [1].

- Object: neutrinoless double-beta ( $0\nu\beta\beta$ ) decay

**MAJORANA:** Based on the work of previous experiments (e.g. **Heidelberg-Moscow Experiment**), the MAJORANA collaboration aims to observe  $0\nu\beta\beta$  events from the decay of  $^{76}\text{Ge}$  embedded in high purity germanium detectors. If there is  $0\nu\beta\beta$  decay it will be visible as a small spike at the end of the beta spectrum.

This list of experiments is by no means complete. It is only meant to demonstrate that neutrino physics is a very active research field.

## 1.2 Neutrino Detection with Organic Scintillators

There are two types of weak interactions that are utilized in neutrino detectors:

- Neutral current (NC) interactions: As the neutrino travels through the detector, it transfers part of its energy and momentum to another particle before leaving the detector. Depending on the energy/momentum transfer, the target particle might be accelerated to relativistic speeds. In the case of a relativistic charged target particle, Cherenkov light is emitted along the track in the medium. This light can then be measured with e.g. photomultiplier tubes. Each of the three neutrino flavors can take part in a NC interaction. The drawback is the indistinguishability of neutrino flavor in this type of detection.
- Charged current (CC) interactions: A neutrino can produce its massive electrically charged partner if it can provide enough energy to generate its mass. A neutrino experiment based on charged current interactions therefore needs to have neutrinos of sufficient energy. Artificially creating such energies with colliders can be a huge challenge. Unlike in NC interaction, the target particle changes its identity. The interaction used in the Daya Bay experiment is the inverse  $\beta$ -decay  $\bar{\nu}_e + p \rightarrow n + e^+$  reaction. As the positron annihilates with an electron, and as the neutron is later captured on a gadolinium (or some other) nucleus, flashes of light are produced. Both flashes are detected by photomultiplier tubes, and the coincidence is used as a unique signature for a neutrino event.

### 1.2.1 Principle of Detection

Organic liquid scintillator (LS) can be used to detect neutrinos via the inverse  $\beta$ -decay reaction. In such a reaction, the neutrino produces a neutron and a positron inside the LS. These two particles generate a 'prompt' and a 'delayed' signal. The fast signal originates from ionization

produced by the positron and its annihilation with an electron of the LS. From the positrons energy it is possible to calculate the neutrino's energy:

$$E_\nu \approx E_{e^+} + 0.8\text{MeV} \quad (11)$$

Equation (11) results from the energy conservation law and the masses of the proton and neutron. In an inverse  $\beta$ -decay reaction, a proton converts into a neutron and a positron is emitted. The mass difference between the neutron and positron-plus-electron is  $\sim 0.8$  MeV while the mass of the neutrino is negligible. To determine the positron's energy, one first has to measure the LS light output generated by ionization and by the gammas coming from the positron annihilation. These gammas, if energetic enough, lead to pair production and, at a later stage with less energy, to Compton scattering inside the scintillator. During these processes charged particles ( $e^+$  and  $e^-$ ) travel through the scintillator and excite the scintillator molecules which then emit light.

Another key aspect of neutrino detection is to measure the 'delayed' signal, which provides a great signature for background rejection. This second signal originates from the capture of the neutron on a nucleus. In this reaction the nucleus emits a few high energy gamma rays (the energy and number of which depend on the capturing isotope). The mean capture time depends on the composition of the liquid scintillator. In the Daya Bay experiment, gadolinium has been added to the LS to decrease the mean capture time from  $\sim 200\mu\text{s}$  to  $\sim 26\mu\text{s}$  and to increase the capture energy from 2.2 to 8 MeV.

The light emitted by a scintillator's molecules is usually wavelength shifted before being detected by photomultiplier tubes that convert light output into electrical signals that can be easily recorded. The light output of the scintillator molecules is nonlinear and depends on the energy of the electrons. Knowledge of the nonlinearity of the LS is crucial for any experiment deploying scintillator materials. The measurement of this nonlinearity is the topic of this thesis.

### 1.2.2 Process of Light Generation

The last chapter described how an electron anti-neutrino produces positrons and electrons in the LS. To understand how organic liquid scintillators convert the energy of these particles into light, one has to look at the smallest relevant molecular substructure, the benzene ring. A benzene ring is made up of hydrogen (electron configuration:  $1s^1$ ) and carbon atoms (electron configuration:  $1s^2 2s^2 2p^2$ ). The left illustration in figure 5 shows a benzene ring structure.

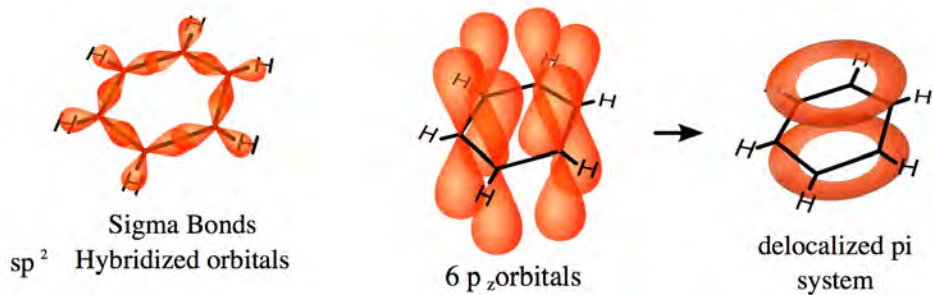


Figure 5: Atomic and molecular orbitals of a benzene ring structure[9]

Each of the carbon atoms at the 6 corners of the benzene ring has three bonds, one to the hydrogen atom and two to the neighboring carbon atoms. Since carbon in the ground state only has two valence electrons available for bonding it needs to promote one of the  $2s$  electrons into the  $2p$  orbital. This results in 4 unpaired electrons ( $2s$ ,  $2p_x$ ,  $2p_y$  and  $2p_z$ ). Atoms always strive for maximum bonding strength. In case of the benzene ring maximum bonding strength between

carbon and hydrogen atoms is achieved through three  $\sigma$ -bonds separated by  $120^\circ$ .  $\sigma$ -bonds are covalent bonds that are characterized by a big head-to-head overlap of two atomic orbitals (shown in the left illustration of figure 5). To form the required orbital geometry for the bonds, the s- and p-orbitals hybridize. Hybridization is a process in which the atom superimposes its orbitals to form the desired orbital geometry. In the case of the benzene ring, only the  $2s$ ,  $2p_x$  and  $2p_y$  orbitals get hybridized to form the three bonds. The fourth orbital,  $2p_z$ , remains unchanged. After all bonds have been formed, the  $2p_z$  orbitals form a structure that is illustrated in the center of figure 5. The  $2p_z$  orbitals actually overlap sideways, but this is not shown in the illustration. These sideways overlaps of orbitals form a  $\pi$ -system. A  $\pi$ -system is an accumulation of  $\pi$ -bonds in which the electrons are delocalized over the whole ring structure. The right illustration in figure 5 shows one of the three newly formed molecular orbits in which the  $2p_z$  electrons now reside.  $\pi$ -bonds, which in benzene form a resonant structure, are much weaker than  $\sigma$ -bonds and can therefore be much more easily excited. Figure 6 shows the energy levels of an electron inside a  $\pi$ -system.

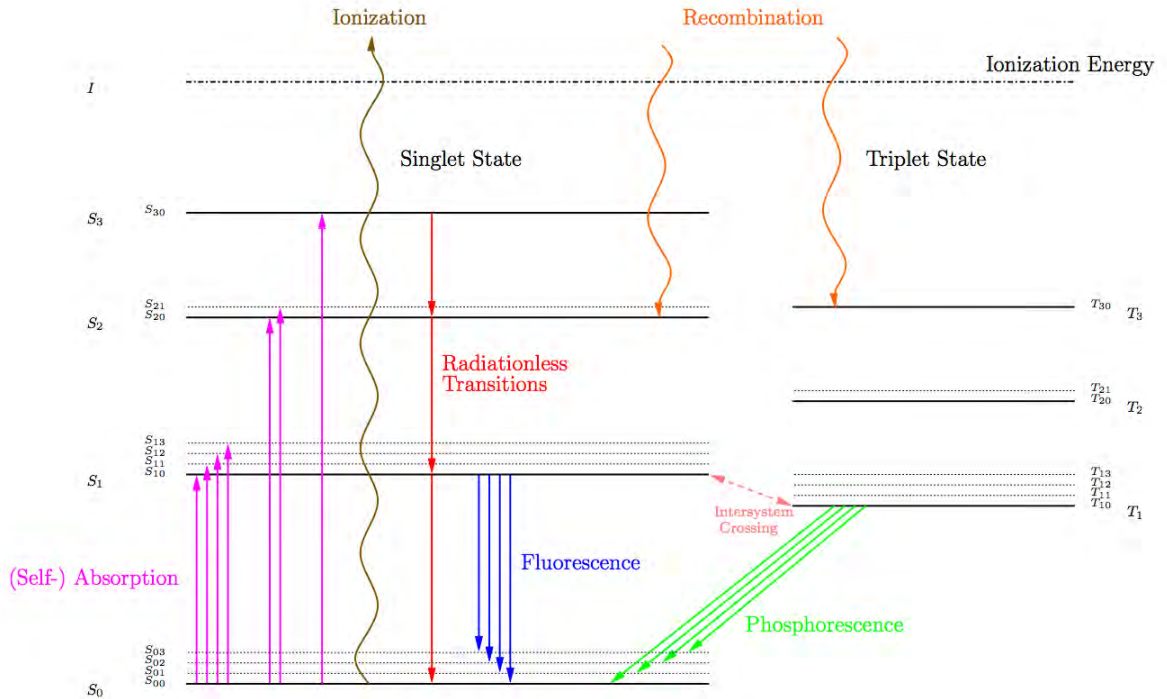


Figure 6: Diagram describing the various energy levels of electrons in the  $\pi$  system of an organic scintillator[20]

Depending on the energies of the electrons and positrons generated in the LS, they will either excite (pink lines), ionize (brown wavy lines), or do nothing to the molecules of the LS. The thick black horizontal lines denote the energy levels of discrete singlet spin states ( $S_1 - S_3$ ) and triplet spin states ( $T_1 - T_3$ ). The thin black horizontal lines that come along with singlet and triplet spin states are vibrational levels of that state. In order to emit light, a molecule in the ground state has to be excited with an energy that is at least the difference in energies between the highest vibrational ground state and the first spin singlet state. These energies are on the order of 2 - 4.5 eV, while vibrational states only have a sub-eV spacing.

The only states that can actually emit light are  $S_1$  and  $T_1$ . Compared to the  $S_1$  state, which dissipates its energy via fluorescence (the fast form of luminescence,  $\tau \sim ns$ ), the relaxation from  $T_1$  to the ground states is forbidden by the selection rules of electronic transitions and is therefore highly suppressed (phosphorescence, the slow form of luminescence,  $\tau \sim ms$ ). Alternatively, the

electron could switch back from the  $T_1$  to the  $S_1$  state, but this would require it to gain the energy for a spin flip from collisions with other molecules.

Vibrational states and states higher than  $S_1$  and  $T_1$  dissipate their energy radiationless in the form of heat until they either reach the ground state or  $S_1/T_1$ . This also leads to different light wavelengths for the different vibrational levels of the ground state that the electron can fall back to. The vibrational state  $S_{03}$  is at a higher energy level than e.g.  $S_{01}$ ; therefore, the emitted light will be less energetic if the electron ends up in this state.

### 1.2.3 Quenching

The focus of this thesis is to determine the liquid scintillator's nonlinearity of light emission in response to electrons; therefore, some mechanisms that might contribute to this nonlinearity should be discussed. In general, anything that reduces fluorescence is considered quenching. Quenching has two main causes: Either the scintillating component is kept from reaching its excited state, or excited states dissipate their energy non-radiatively. These processes are in general energy-dependent, and lead to an energy dependent nonlinearity in the light yield of a scintillator.

Some known effects are:

- **Ionization quenching**

When an ionizing particle travels through a scintillator, it ionizes the scintillator's molecules in its path. These ionized molecules do not participate in the fluorescence process and are therefore called 'damaged'. The higher the stopping power and energy of a particle, the more the molecules are ionized, and thus the stronger is this effect. There can be light emission when the molecular ion recombines with an electron.

- **Kasha's rule**

When scintillator molecules are excited to higher states than the lowest excited electronic state, this energy is effectively lost since these states do not participate in the emission of visible photons. The effect can be seen in figure 6, where visible fluorescence and phosphorescence only occur between  $S_1$ ,  $T_1$  and  $S_0$ .

- **Dynamic quenching**

Newly excited molecules can collide with neighboring molecules. If this happens, the excited molecule de-excites without emission of photons.

- **Resonant energy transfer**

The energy of an excited molecule can be transferred non-radiatively to a second molecule, thereby reducing the fluorescence of the primary one. To counteract this, wavelength shifters are added to the LS. The wavelength-shifting molecules absorb the energy that another molecule dissipates either via collisions or through photons, and re-emits it in the form of lower energy photons. These photons do not have the energy to re-excite another scintillator molecule and can therefore leave the scintillator volume easily.

- **Temperature rise**

Part of the incident particle's energy is lost in elastic and inelastic interactions that generate heat.

- **Cherenkov light** If a charged particle in a material travels faster than the speed of light within that material, part of its energy is lost by Cherenkov light generation.

In general, these effects sum up to a material-, particle-, and energy-dependent nonlinearity, one which cannot be well described theoretically, and thus must instead be measured. One semi-empirical model that describes the differential light output of a scintillator is Birk's law:

$$\frac{dL}{dx} = \frac{L_0 \cdot \frac{dE}{dx}}{1 + kB \cdot \frac{dE}{dx}} \quad (12)$$

$\frac{dL}{dx}$  is the light yield per path length, which depends on the absolute light yield constant  $L_0$ , the energy deposition per unit length  $\frac{dE}{dx}$ , and the Birk's factor  $kB$ , which describes the density of 'damaged' molecules per energy deposition length. The constants in the equation differ for different scintillators and particles. For a heavy charged particle,  $\frac{dE}{dx}$  can be described by the Bethe-Bloch formula. For light particles like electrons, additional effects (exchange interactions, Bremsstrahlung, density corrections) have to be taken into account. Recombination also plays a dominant role.

Measuring the absolute light yield is a complicated task that requires a  $4\pi$  collection of the light emitted by the scintillator. For many experiments (e.g. Daya Bay), a relative measurement of the light yield between detectors is sufficient. In general, most of the light emission of a liquid scintillator is isotropic, but measurements of the relative light yield have to be done with great care because some components can be directional (e.g. Cherenkov light).

One thing to mention here is that in the measurements conducted in this work, the light-producing electrons in the LS were generated by Compton-scattered photons. In Daya Bay, positrons are produced by the inverse beta decay reaction. These positrons then annihilate to two gammas which then produce electrons in Compton scattering events. Due to the small magnitude of the difference between positron and electron quenching, the obtained result can be used for both electrons and positrons.

### 1.3 Daya Bay Experiment

The Daya Bay experiment is a reactor based neutrino oscillation experiment located 50 km north of Hong Kong in the province of Guangdong, mainland China. Its goal is to make a precise measurement of the mixing angle  $\theta_{13}$ . Its predecessors were the CHOOZ and Palo Verde neutrino oscillation experiments. In contrast to the Palo Verde experiment's results, which were dominated by systematic errors[7], the CHOOZ experiment was able to set a limit on  $\sin^2(2\theta_{13}) \leq 0.17$  at a 90% confidence level[5].

The Daya Bay experiment started data taking at the end of 2011 and will continue until the end of 2017. It is an international collaboration involving about 230 collaborators, mainly from China and the USA. The most recent Daya Bay results from August 12, 2014 show that  $\sin^2(2\theta_{13}) = 0.090^{+0.008}_{-0.009}$  and  $|\Delta m_{ee}^2| = (2.59^{+0.19}_{-0.20}) \times 10^{-3} eV^2$ [4].

Eight identical detectors are located at different positions around the 6 powerful reactor cores of the Guangdong Nuclear Power Group that produce a total thermal power of 17.4 GW. The detectors are located in 2 subterranean near halls, namely 'Daya Bay Near' and 'Ling Ao Near,' and one far hall called the 'Far Site'. To suppress cosmic rays, the two near halls have an overburden of about 100m rock (equivalent to 270m water), and the far hall has a rock overburden of 350m (equivalent to 860m water). The layout is shown in figure 7.

Half of the detectors are used as near detectors, at mean distances of 365 and 500 m, to measure the flux and spectrum of the electron anti-neutrinos produced in the reactor cores. The other detectors are placed at a mean distance of 1600 m, where the largest oscillation probability is expected. Any deficit in neutrino flux at the far site that is greater than the expected  $\frac{1}{L^2}$  decline is a signature for neutrino oscillations and is used to extract  $\theta_{13}$  and  $\Delta m_{ee}^2$ , as demonstrated in section 1.3.3.

The use of multiple detectors at each location provides a powerful check of detector performance, and their deployment at near and far sites makes the results largely independent of the absolute

neutrino flux. To carry out this high precision measurement, systematic errors and backgrounds have to be known to a sub-percent level, which makes it essential to measure the scintillator's nonlinearity of light emission. Section 1.3.2 explains how electron anti-neutrinos are measured. It should also give an idea of how the energy of the neutrinos is determined and why the knowledge of the nonlinearity is crucial for Daya Bay's analysis results.

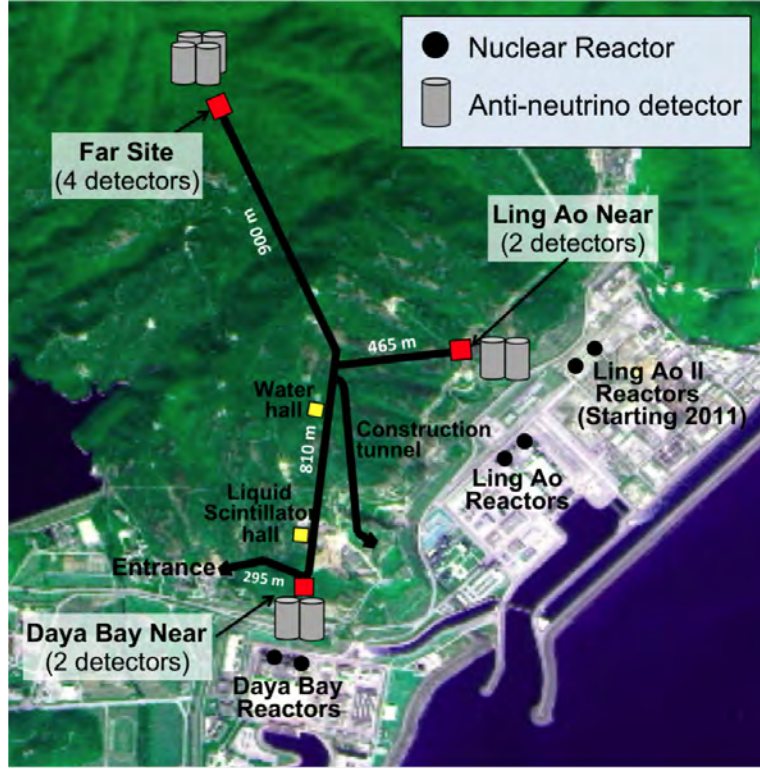


Figure 7: Layout of the detectors around the Guangdong nuclear power station

### 1.3.1 Neutrino Detection Medium

The Daya Bay experiment uses gadolinium-doped linear alkylbenzene (Gd-doped LAB) as the detection medium, in which electron anti-neutrinos are detected via the inverse  $\beta$ -decay reaction. Linear alkylbenzene (LAB) consists of a straight chain of 10-13 carbon atoms attached to a benzene ring[6]. LAB has a low chemical reactivity and a light yield comparable to other scintillators. The LS is doped with 0.1 % (mass) gadolinium to increase the cross section for neutron capture, thus decreasing the capture time from  $\sim 200 \mu s$  to  $\sim 28 \mu s$ .

Even though a majority of the scintillator is made up of hydrogen and carbon atoms, the capture probability on either of those elements is small compared to the one on Gd. The reason lies in gadolinium's large cross section for neutron capture of 49,000 barn (hydrogen: 0.332 barn). To dissolve Gd in the LS, 3,5,5-trimethylhexanoic acid (TMHA) is used as a ligand due to its easy production and good stability in LAB. Other additives include  $\frac{3g}{l}$  2,5-diphenyloxazole (PPO) as a fluor and  $\frac{15mg}{l}$  p-bis-(o-methylstyryl)-benzene (bis-MSB) as a wavelength shifter. The purpose of adding additional fluor (PPO) is to increase the light output.

In total,  $\sim 185$  tons of the 0.1 % Gd-LS have been produced for the Daya Bay experiment. Lawrence Berkeley National Laboratory has a large selection of different samples that were

taken during production. All of the samples should have the same chemical characteristics as they were all taken from the same mixing tank. This work uses a sample from 2011.

### 1.3.2 Detector Design

Anti-neutrinos are detected via the inverse-beta decay reaction in the gadolinium-loaded liquid scintillator (Gd-LS):

$$\bar{\nu}_e + p \rightarrow n + e^+ \quad (13)$$

The positron produces a prompt signal that is followed by a delayed signal caused by the neutron's capture on a gadolinium nucleus, as illustrated in figure 8. The prompt positron signal is directly related to the anti-neutrino energy ( $E_{\bar{\nu}_e} \approx E_{e^+} + 0.8 \text{ MeV}$ ), but the measurement requires a very good knowledge of the scintillator's characteristics. The delayed signal originating from the neutron's capture on gadolinium releases 8 MeV in a cascade of 3-4  $\gamma$  rays.

Gd-doping has two advantages for the experiment: The neutron capture time is shortened from  $\sim 200 \mu\text{s}$  to  $\sim 28 \mu\text{s}$  and its 8 MeV signal is much cleaner than the 2.2 MeV signal from capture on hydrogen. These characteristics give an anti-neutrino event a distinct signature and help to reduce accidental backgrounds by a factor of 7.

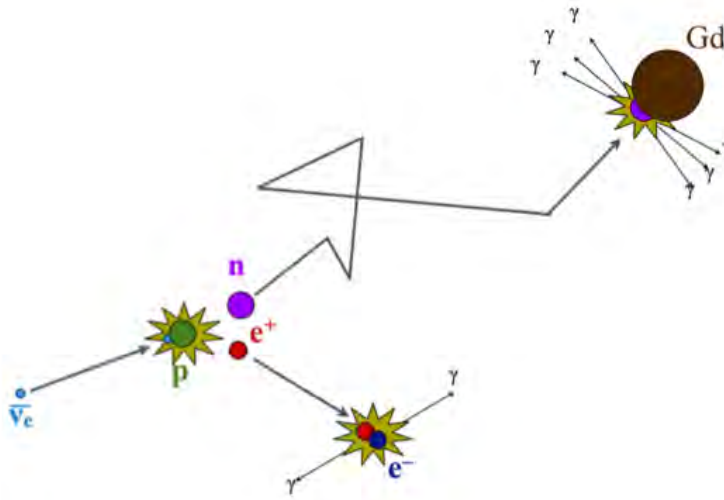


Figure 8: Electron anti-neutrino signature

To reduce detector-related systematic errors, all 8 detectors are designed, built, and calibrated identically. The Daya Bay anti-neutrino detectors are split into three zones separated by acrylic vessels as shown in figure 9. The inner vessel holds the actual neutrino target, 20 tons of 0.1 % Gd-LS. The outer acrylic vessel, surrounding the inner one, holds 20 tons of undoped LS and acts as a gamma catcher for gammas escaping from the target zone. Finally the outermost zone is filled with mineral oil and surrounded by 192 photomultiplier tubes (PMTs). Two reflectors located at the top and bottom are used to increase the light collecting efficiency. The mineral oil shields the inner area from external sources of background. Calibration is done by deploying radioactive sources and light emitting diodes (LEDs) into the active regions of the detectors.

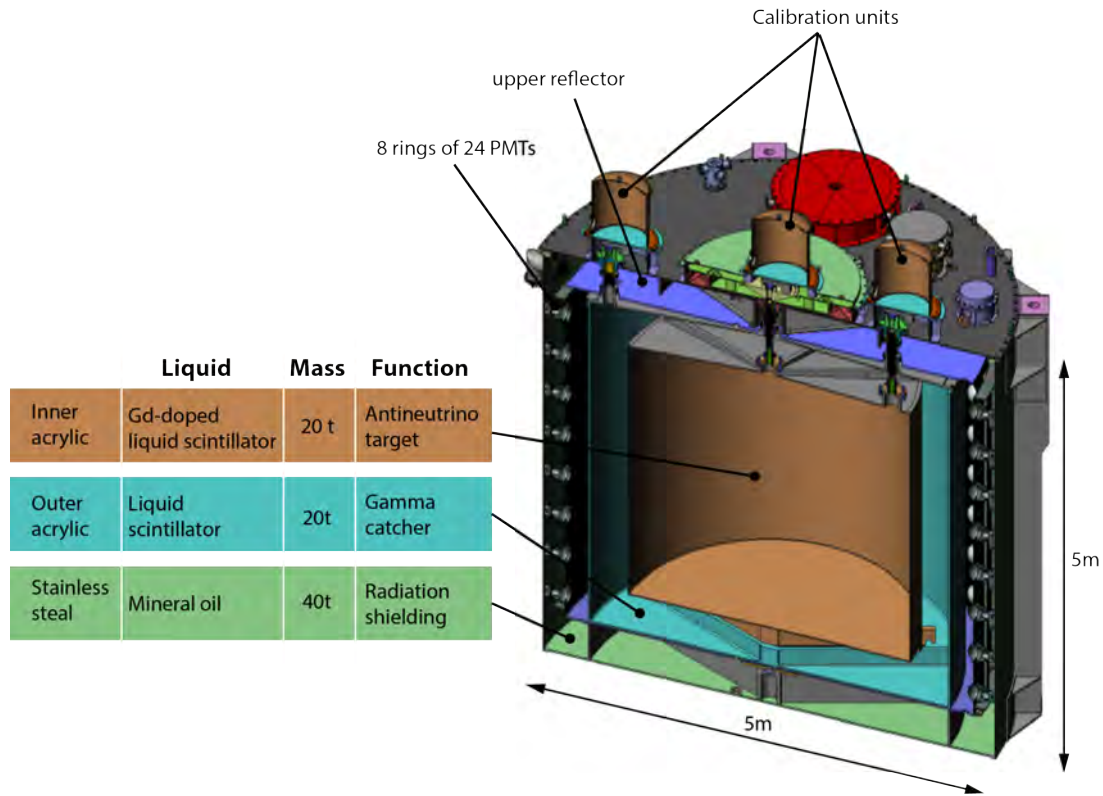


Figure 9: Daya Bay anti-neutrino detector design

All detectors are immersed in an instrumented water pool (see figure 11), which serves two main purposes: First it attenuates gammas coming from ambient radioactivity as well as neutrons produced by cosmic rays. Secondly, it is used to tag cosmic ray muons by detecting the Cherenkov light produced by them as they pass through the water. Each pool is divided into two optically decoupled regions as shown in figure 10: the outer water shield and the inner water shield. This design increases redundancy and efficiency in detecting background signals such as muons, where the detection efficiency is 99.9 %.

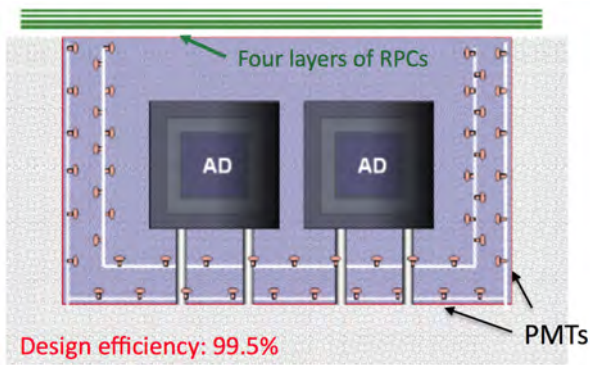


Figure 10: Cross-section of a pool



Figure 11: Water pool during construction

Additional, further cosmic muon tagging is provided by multiple layers of resistive plate chambers (RPCs). The RPCs are mounted on top of the pool and can be retracted when not in use. Figure 10 shows one pool covered with RPCs while the other one is open.

### 1.3.3 Data Analysis

During data analysis, the number of detected electron anti-neutrinos in the near detector is compared to the number of detected electron anti-neutrinos in the far detector. From the number of neutrinos that have vanished and the distortion of the spectrum, one can then calculate  $\theta_{13}$  and  $\Delta m_{ee}^2$ .

The neutrinos are produced in nuclear fission processes inside the six reactors of the Guangdong Nuclear Power Group. In full operation, roughly 6 anti-neutrinos are released per fission. The total fission rate from all reactors is  $6 \times 10^{20} s^{-1}$  leading to an total isotropic electron anti-neutrino flux of about  $36 \times 10^{20} s^{-1}$ . Electron anti-neutrinos coming from different fissioning isotopes have different rates and energy spectra, as shown in figure 12.

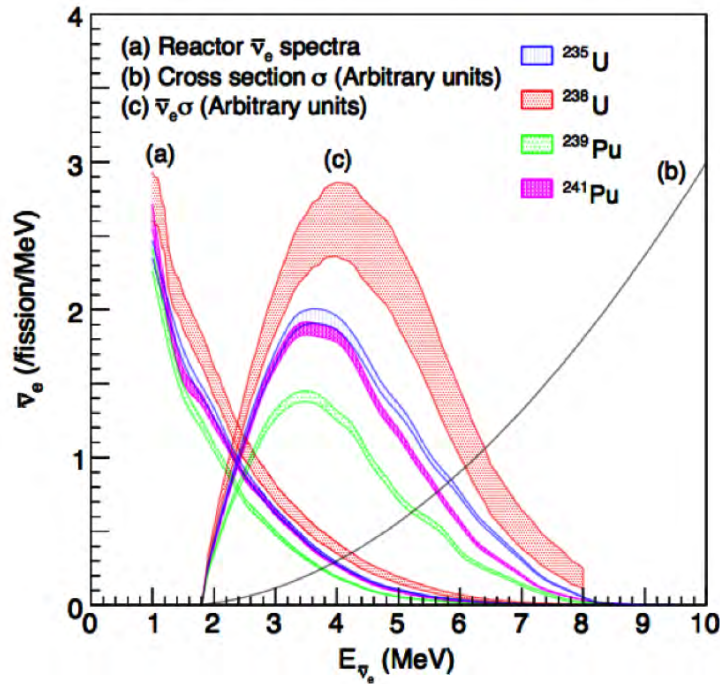


Figure 12: Reactor  $\bar{\nu}_e$  spectra

As can be seen in figure 12 (from the ILL Grenoble measurement), there are large systematic uncertainties in the reactor anti-neutrino flux, ranging from 3 to 5 %. This has been the largest uncertainty in previous reactor neutrino oscillation experiments. Daya Bay uses a method, first suggested in 1999[22], that relies on a relative measurement between near and far detectors to cancel out this uncertainty. This approach results in equation (14), which describes the ratio in neutrino flux between far and near detectors as a function of detector target mass ( $N_{p,f}$ ,  $N_{p,n}$ ), distance from the reactor ( $L_n$ ,  $L_f$ ), detector efficiency ( $\epsilon_f$ ,  $\epsilon_n$ ), and survival probability of an electron anti-neutrino ( $P(E, L_f)$ ,  $P(E, L_n)$ ).

$$\frac{N_f}{N_n} = \left( \frac{N_{p,f}}{N_{p,n}} \right) \left( \frac{L_n}{L_f} \right)^2 \left( \frac{\epsilon_f}{\epsilon_n} \right) \left[ \frac{P(E, L_f)}{P(E, L_n)} \right] \quad (14)$$

The detectors are almost identical, but since their masses are slightly different (sub-percent level), and reactor operating times are different, the relative detector efficiencies vary slightly and do not cancel out completely. The last part in equation (14) is the ratio of electron anti-neutrino survival probability for different distances as a function of neutrino energy. The probability  $P_{\bar{\nu}_e \rightarrow \bar{\nu}_e}$  that an electron anti-neutrino survives the journey between detectors reads:

$$P_{\bar{\nu}_e \rightarrow \bar{\nu}_e} = 1 - \sin^2(2\theta_{13})\sin^2\left(\Delta m_{ee}^2 \frac{L}{4E}\right) - \sin^2(2\theta_{12})\cos^4(\theta_{13})\sin^2\left(\Delta m_{21}^2 \frac{L}{4E}\right) \quad (15)$$

Equation (14) shows that, in principle, two detectors at different distances from one reactor core would be sufficient to obtain results. However, measurements with small statistical and systematical error require multiple detectors around more than one reactor core. There are several approaches for how to deal with multiple reactor cores and detectors. The approach chosen by the Daya Bay group at LBNL is to sum up the contributions for each detector hall and then compare the different halls to each other in order to obtain a result.

### Analysis Step-by-Step

Neutrinos are detected by their unique signature, as described in section 1.3.2, but some further cuts have to be applied to select inverse beta decay (IBD) candidates:

- Events caused by spontaneous PMT light emissions ("flashers") are rejected.
- The energy of the prompt positron, which carries information about the neutrino's energy, has to be within 0.7 to 12 MeV.
- The energy of the delayed neutron has to be within 6.0 to 12 MeV, i.e., only Gd captures are used.
- The neutron capture time has to be between  $1\mu s$  and  $200\mu s$ .
- Vetoes are applied in response to various muon signatures. A water pool muon ( $>12$  PMT hits in each water pool) results in the rejection of events that occur in a time window between  $2\mu s$  before and  $600\mu s$  after the muon. A muon that makes its way into the AD ( $>3000$  photo-electrons produced) leads to a rejection window of  $-2\mu s$  to  $1400\mu s$ . The longest veto is caused by an AD shower muon ( $> 3 \times 10^5$  photo-electrons). Here the window is  $-2\mu s$  to  $0.4s$ .
- There should be no additional prompt-like signals  $400\mu s$  before and no additional delayed-like signal  $200\mu s$  after the delayed neutron capture. This eliminates ambiguous events.

A plot of prompt energy vs. delayed energy is shown in figure 13. The events of interest are marked with a red box. The projection of these events onto the prompt reconstructed anti-neutrino energy axis is shown in figure 14.

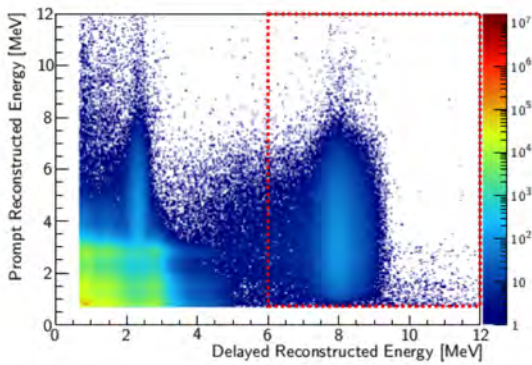


Figure 13: Events after selection

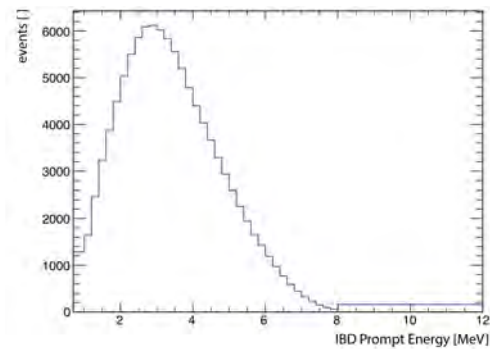


Figure 14: Projection of IBD events

The prompt energy spectrum in figure 14 needs to be corrected for backgrounds and the efficiency of the detectors, so as to ensure comparable spectra between the halls. The background to subtract from the spectrum is a composition of multiple backgrounds as shown in figure 15, which were determined by Monte Carlo simulations as well as *in situ* measurements.

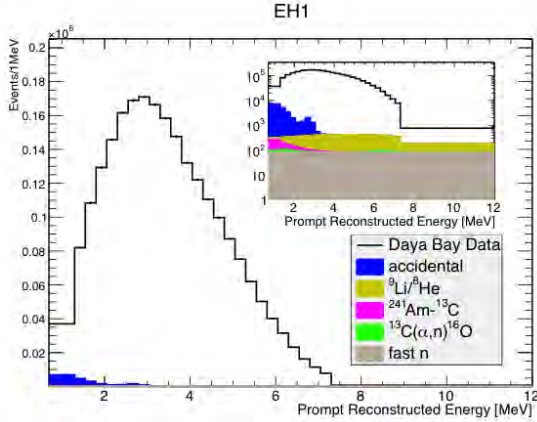


Figure 15: Backgrounds that are subtracted from the spectrum

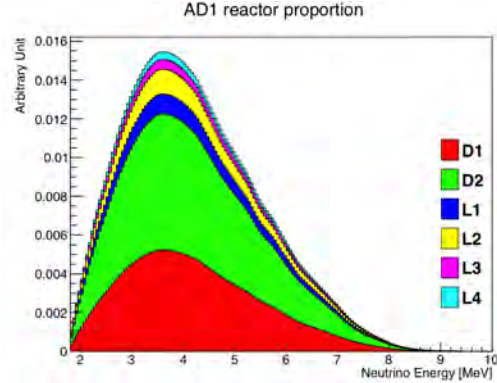


Figure 16: Contribution of each reactor to the spectrum

The efficiency correction includes effects based on detector livetime, target mass, muon rate, multiplicity cut, and prompt/delayed energy cuts. After the spectrum has been corrected, it is converted from IBD prompt energy (charge from PMTs) to anti-neutrino energy. This is done by a matrix describing the detector's response. The matrix includes boundary effects of the acrylic vessel, the energy resolution, and scintillator and electronics nonlinearity. To a large extent, these effects were simulated with Monte Carlo programs. After the neutrino spectrum has been reconstructed from the positron spectrum, the contribution of each reactor core to the neutrino spectrum is studied (see figure 16).

To do this, each reactor's operating state (current power setting and isotope composition), reactor-detector baseline, and theoretical reactor  $\bar{\nu}_e$  spectrum is required. With contributions of each reactor known, the near sites can be used to predict the flux at the far sites assuming a simple  $\frac{1}{L^2}$  dependence. A so-called shape analysis is then done for each of the 37 energy bins of the neutrino spectrum. A summary of event counts for each detector in the three halls, together with their estimated backgrounds, is given in table 1. EH1, EH2 and EH3 stand for 'Ling Ao Near', 'Daya Bay Near', and 'Far Site', respectively.

The Daya Bay experiment has gone through two data taking periods so far, one with 6 detectors, from December 2011 to August 2012, and another one with 8 detectors, from October 2012 to December 2013, referred to as the 6AD and 8AD periods. In the data analysis for the 8AD period, a bigger covariance matrix (as explained shortly) is used to account for the additional detectors and other effects that have arisen from the upgrade. The preliminary results for the 8AD period are shown in figures 17 and 18 [1].

The predicted and observed flux for the near and far halls are compared to find the best oscillation parameters that can account for the deficit.

The  $\chi^2$  function for fitting the oscillation parameters  $\Delta m_{ee}^2$  and  $\sin^2(2\theta_{13})$  is constructed as:

$$\chi^2 = \sum_{i,j}^{bins} (F_i^{obs} - F_i^{pred}(\Delta m^2, \sin^2(\theta_{13}))) V_{i,j}^{-1} (F_j^{obs} - F_j^{pred}(\Delta m^2, \sin^2(\theta_{13}))) \quad (16)$$

	EH1		EH2	EH3		
	AD1	AD2	AD3	AD4	AD5	AD6
IBD candidates	101290	102519	92912	13964	13894	13731
DAQ live time (days)	191.001		189.645	189.779		
$\epsilon_\mu \cdot \epsilon_m$	0.7957	0.7927	0.8282	0.9577	0.9568	0.9566
Accidentals (per day)	9.54±0.03	9.36±0.03	7.44±0.02	2.96 ± 0.01	2.92 ± 0.01	2.87 ± 0.01
Fast-neutron (per AD per day)	0.92±0.46		0.62±0.31	0.04±0.02		
$^9\text{Li}/^8\text{He}$ (per AD per day)	2.40±0.86		1.20±0.63	0.22±0.06		
Am-C correlated (per AD per day)	0.26±0.12					
$^{13}\text{C}(\alpha, n)^{16}\text{O}$ background (per day)	0.08±0.04	0.07±0.04	0.05±0.03	0.04±0.02	0.04±0.02	0.04±0.02
IBD rate (per day)	653.30±2.31	664.15±2.33	581.97±2.07	73.31 ± 0.66	73.03 ± 0.66	72.20 ± 0.66

Table 1: IBD candidates for different halls (EH1 - EH3) and detectors (AD1 - AD6)

Where  $F_i^{pred}$  ( $F_i^{obs}$ ) is the predicted (observed) number of events in energy bin  $i$  at the far site.  $V_{i,j}$  is the covariance matrix that contains all systematic and statistical errors. The covariance matrix  $V = V_{sig} + V_{bkg} + V_{stat}$  is composed of three parts that represent the systematic uncertainties of the IBD signal, those of the background, and the statistical error. The correlation between the errors are determined using sophisticated Monte Carlos simulations.

Below are the latest results of the Daya Bay experiment[1]:

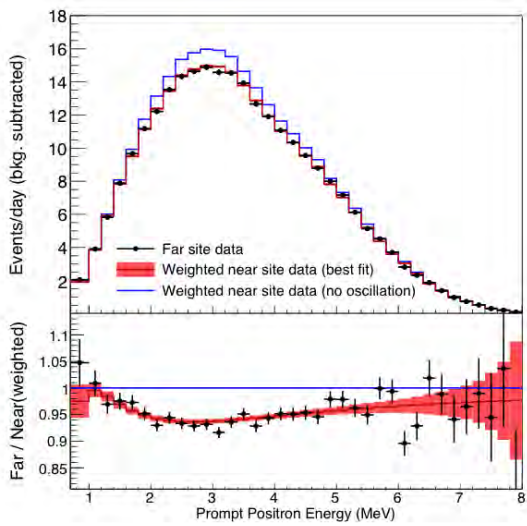


Figure 17: Comparison between far and near spectrum

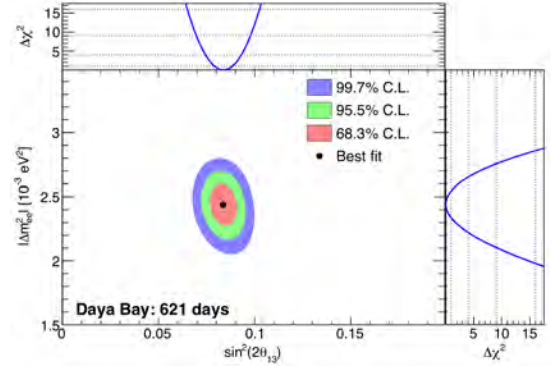


Figure 18: Daya Bay's current result for  $\theta_{13}$  and  $\Delta m_{ee}^2$

Figure 17 shows the spectra from the near and far sites as well as their ratio. The lower plot in figure 17 already includes oscillation effects from  $\Delta m_{ee}^2$  and  $\sin^2(2\theta_{13})$ .  $\Delta m_{ee}^2$  is proportional to the position of the minimum and  $\sin^2(2\theta_{13})$  is proportional to its depth. The result of the fit is shown in figure 18.

## 2 Experimental Method

To measure the energy response for electrons in a liquid scintillator (LS), one needs a way to introduce electrons over a range of energies. The most straightforward option is to use a  $\beta$ -source and place it or dissolve it in the LS volume. This method has the shortcoming that the emitted electrons are not mono-energetic but form a broad beta spectrum, so that the true energy of each electron is unknown.

A smarter way is to use the Compton coincidence method developed by Valentine and Rooney[25], which has been used in many similar measurements[26, 29, 30, 16]. In this method,  $\gamma$ -particles of well defined energy (e.g. from a radioactive source) are shot into the LS volume where some of them undergo Compton scattering against electrons of the LS. By measuring the scattered  $\gamma$ -particle with a high resolution, high purity germanium (HPGe) detector, the deposited energy (the electron's kinetic energy) in the LS can be calculated as  $E_e = E_{\gamma_i} - E_{HPGe}$  where  $E_{\gamma_i}$  is the incident  $\gamma$  energy and  $E_{HPGe}$  is the energy detected by the HPGe detector. The true energy can then be changed by varying the scattering angle. Let us quickly have a look at the derivation of the Compton scattering formula:

The Compton Effect is the elastic scattering of a photon by an electron. In the following derivation, we assume that the electron is at rest when it gets hit by the photon. Furthermore if the binding energy of the electron is much smaller than the photon energy ( $E_e \ll k$ ), as it is in this case, it can be neglected and the electron can be considered as a free particle.

let  $\hbar = c = 1$

$k$  is the initial photon momentum (and energy)

$k'$  is the final photon momentum (and energy)

$E_e = m$  is the initial electron energy

$E'_e$  is the final electron energy

$p'_e$  is the final electron momentum

Energy conservation gives:

$$k + m = k' + E'_e \quad (17)$$

Momentum conservation gives:

$$\vec{k} = \vec{k}' + \vec{p}'_e \quad (18)$$

With the relation  $E'^2_e - p'^2_e = m^2$ , summation and squaring of (17) and (18) gives:

$$(k + m - k')^2 - (\vec{k} - \vec{k}')^2 = m^2 \quad (19)$$

Equation (19) simplified gives:

$$km - mk' - kk' + \vec{k} \cdot \vec{k}' = 0 \quad (20)$$

$\vec{k} \cdot \vec{k}'$  expressed as  $2|\vec{k}||\vec{k}'|\cos(\varphi)$  then gives the energy of the scattered photon:

$$k' = k \frac{m}{m + k(1 - \cos(\varphi))} \quad (21)$$

$1 - \cos(\varphi)$  can be written as  $2\sin^2(\frac{\varphi}{2})$  and gives our final expression for the energy of the scattered photon:

$$k' = k \frac{m}{m + 2k\sin^2(\frac{\varphi}{2})} \quad (22)$$

The kinetic energy of the electron can be calculated as:

$$K'_e = E'_e - m = k - k' = k \left[ 1 - \frac{m}{m + 2k\sin^2(\frac{\varphi}{2})} \right] \quad (23)$$

Equations (22) and (23) are plotted in figure 19 for different gamma sources that might be available for the experiment in the future. Figure 19 illustrates that a considerably smaller (angular) step size at angles below  $60^\circ$  has to be chosen to maintain a similar electron energy spacing between the data points and to avoid gaps in data.

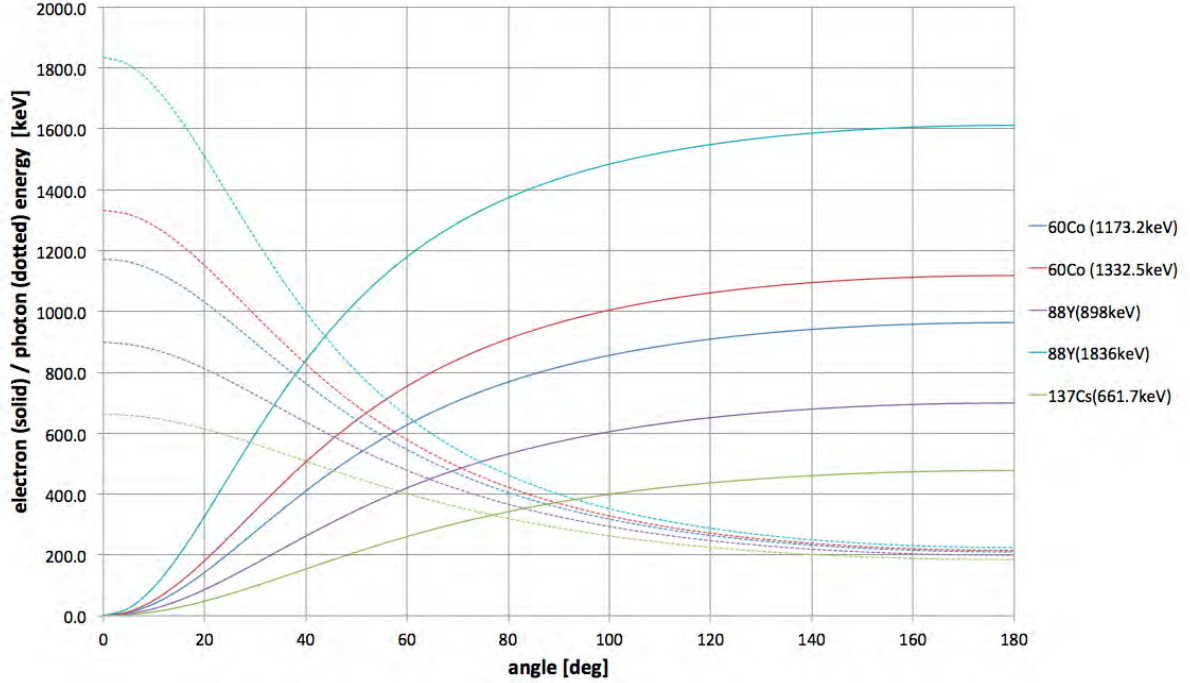


Figure 19: Photon and electron energies for different scattering angles

The Compton spectrometer built for this project can only handle angles between  $20^\circ$  and  $120^\circ$ . This limits the Compton electron's energy to a range of  $\sim 13\%$  to  $\sim 80\%$  of the source's  $\gamma$  energy. One thing to be careful about is the unexpected energy loss of the  $\gamma$  particle on its way to the HPGe detector. This could happen through multiple interactions that do not necessarily all have to happen inside the LS cell. To estimate such effects and design the Compton spectrometer, extensive Geant4 simulations were conducted.

## 2.1 Compton Spectrometer

Figure 20 shows the Compton Spectrometer (CS) that was designed, simulated, and built in the scope of this thesis. The setup consists of a square table which supports a rotating turntable. Mounted on the turntable are the source container, collimators, and radiation catcher. The scattering angle is changed by rotating the source around the LS cell while the cell itself, the post-scattering collimator, and the HPGe detector are stationary. The additional frame that encloses the whole experiment is a support structure for the upper of the two photomultiplier tubes (PMTs), which are mounted on both ends of the cell. To address the problem of reproducibility, a self-centering bolt, held by threads in the turntable, is screwed into one of a series of  $5^\circ$ -spaced holes drilled into the stationary platform. The screw keeps the table top from rotating and allows it to come back to the exact same position.

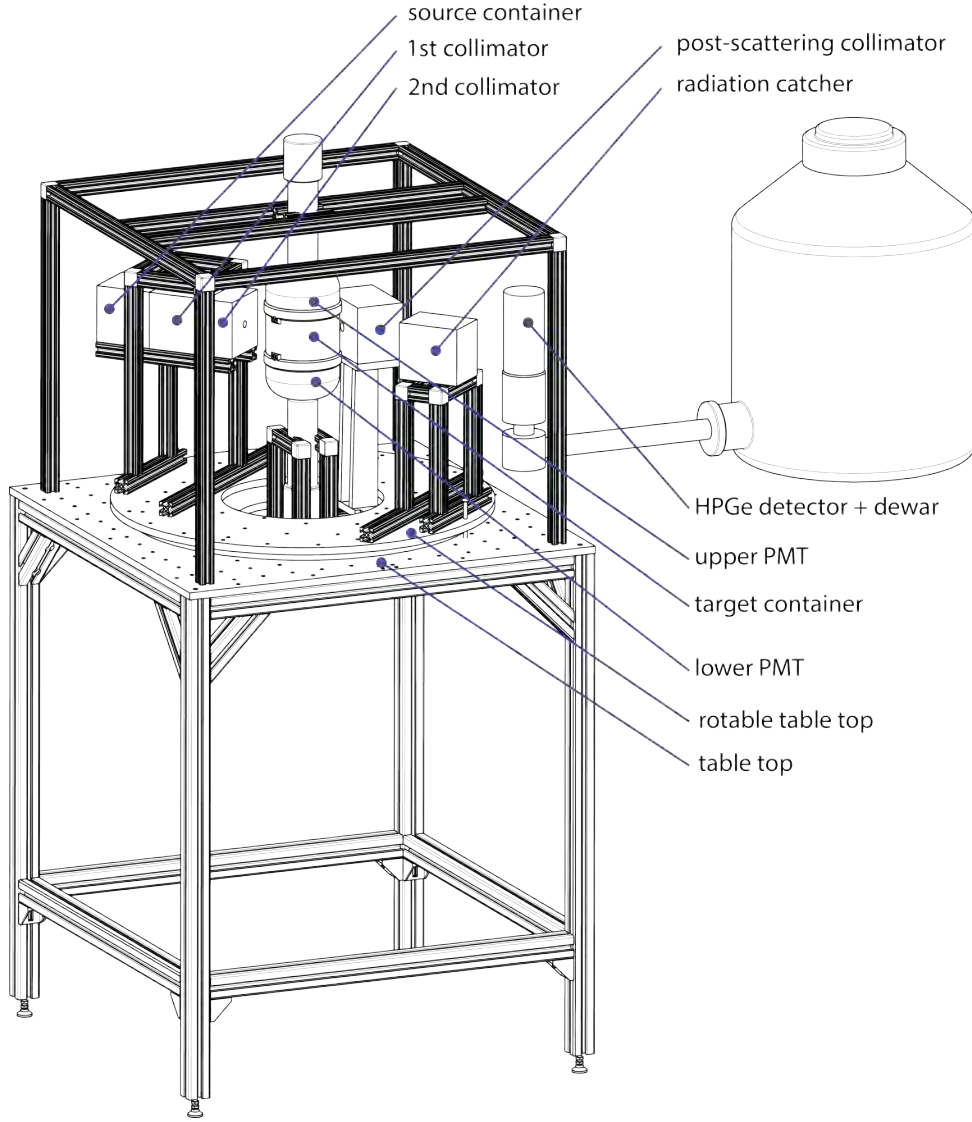


Figure 20: 3D CAD model of the Compton spectrometer

### 2.1.1 Collimators and Source Handling

The source container, collimators, and radiation catcher were first dimensioned with regard to radiation safety before being optimized for the experiment with Geant4 simulations. During dimensioning, equation (24) was used:

$$I_x = I_0 \cdot e^{-\mu x} \quad (24)$$

$I_x$  is the intensity of radiation coming from a source with the intensity  $I_0$  after going a path  $x$  through a material with a linear attenuation coefficient  $\mu$ . The linear attenuation coefficient of lead at an energy that is in the region of available sources ( $^{60}\text{Co}$ ,  $^{137}\text{Cs}$ ) is about  $0.54 \frac{1}{\text{cm}}$ . The consequence is that 99.5 % of the high energy photons coming from the source are absorbed after traveling a distance of 10 cm in lead.

Depending on the strength of the source, the radiation protection requirements, and the requirements of the experiment (direct gamma hits in the HPGe detector are undesirable) the thickness of the shielding had to be adjusted. For the calculations, a point source without the typical  $1/r^2$

effect was assumed. The radiation safety was later verified by Geant4 simulations. The weakest point of the shielding is the gap between the source container and the first collimator. In a later stage of the experiment, this gap was covered by two lead bricks that cut down the dose rate at the sides of the source container, but direct gamma hits from the source are still visible in the data.

After dimensioning the blocks, a Geant4 simulation was set up to find the ideal hole diameter that limits the possible interaction region so as to maximize the event rate while minimizing multiple interactions in the LS and interactions in the acrylic walls. A cross section of the experiment that shows the possible interaction region (red) defined by the collimators can be found in figure 21. The thin red lines represent the most extreme angles at which  $\gamma$ -particles can still successfully pass the collimator (apart from the tiny fraction that have wall interactions inside the collimators' holes).

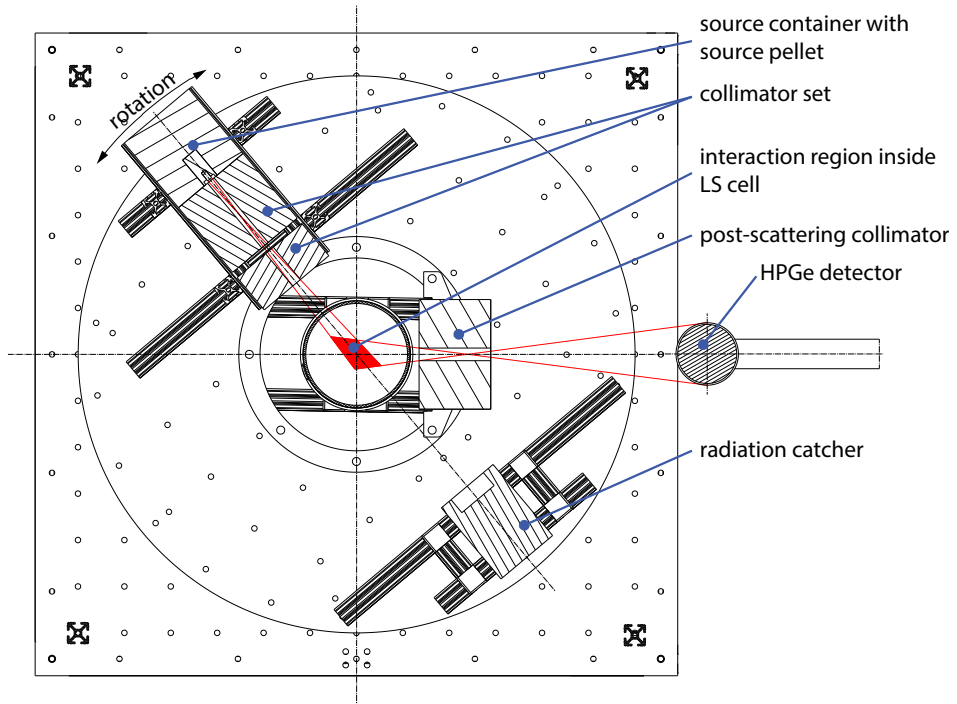


Figure 21: Cross section of Compton spectrometer

The red area in figure 21 shows that the use of only the scattering angle to determine the electron's energy introduces a large systematic error due to the wide range of possible scattering angles (up to  $20^\circ$  per angle position). Assessing possible scattering angles is additionally complicated by gammas that are scattered at small angles inside the collimators. Counteracting this effect requires a special collimator system with two collimators (see figure 22).

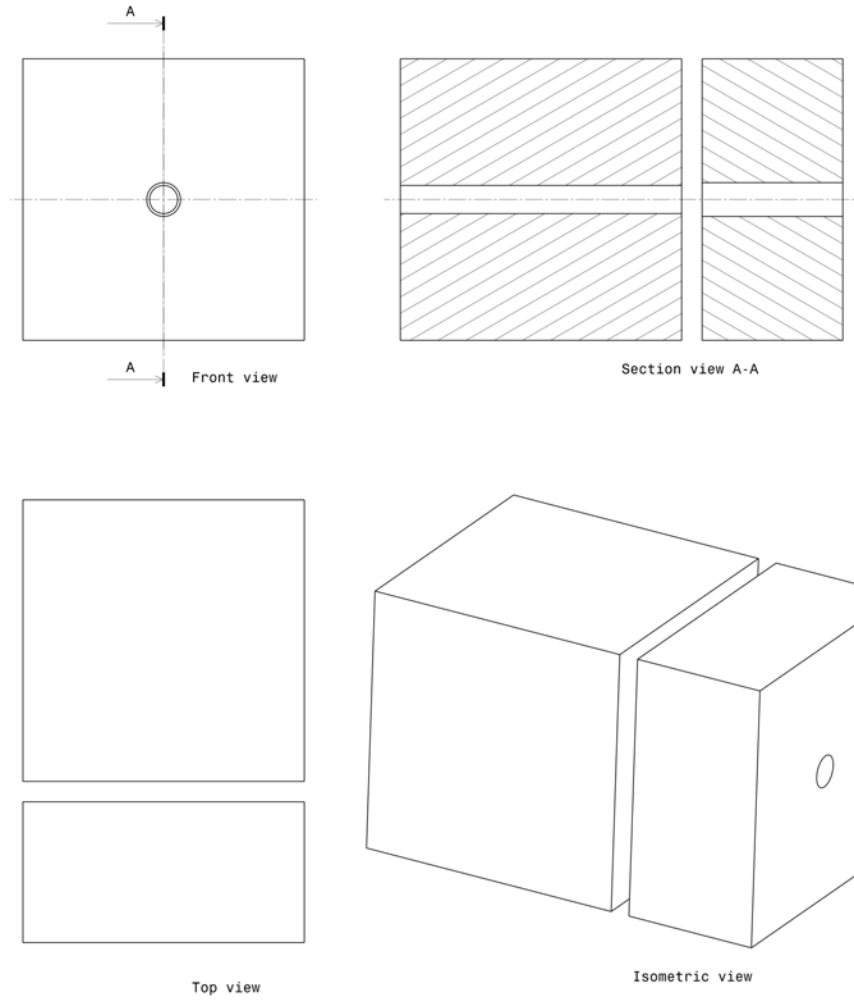


Figure 22: Collimator set

These collimators have slightly different hole diameters. The first collimator has a 10 mm circular hole and does the actual collimation of the gammas coming from the radioactive source. The second collimator follows at a distance of 5-15 mm and has a hole diameter of 12 mm. It absorbs gammas that undergo small angle scattering in the first collimator.

In addition to the collimator set, three different types of post-scattering collimators were manufactured to address different shielding requirements at different angles. The optimal values of the collimator's hole diameter and thickness were also found by Geant4 simulations. Three main factors had to be considered: First, the dose rate at small scattering angles had to be kept down to protect the HPGe detector from too many direct hits. Second, gammas that scattered in the acrylic cell wall had to be shielded from the HPGe detector at all angles to prevent unnecessary backgrounds. Third, the interaction region inside the LS had to be limited to a small area to cut down on multiple scattering events in the data. Figure 23 shows a screenshot of the model used in Geant4.

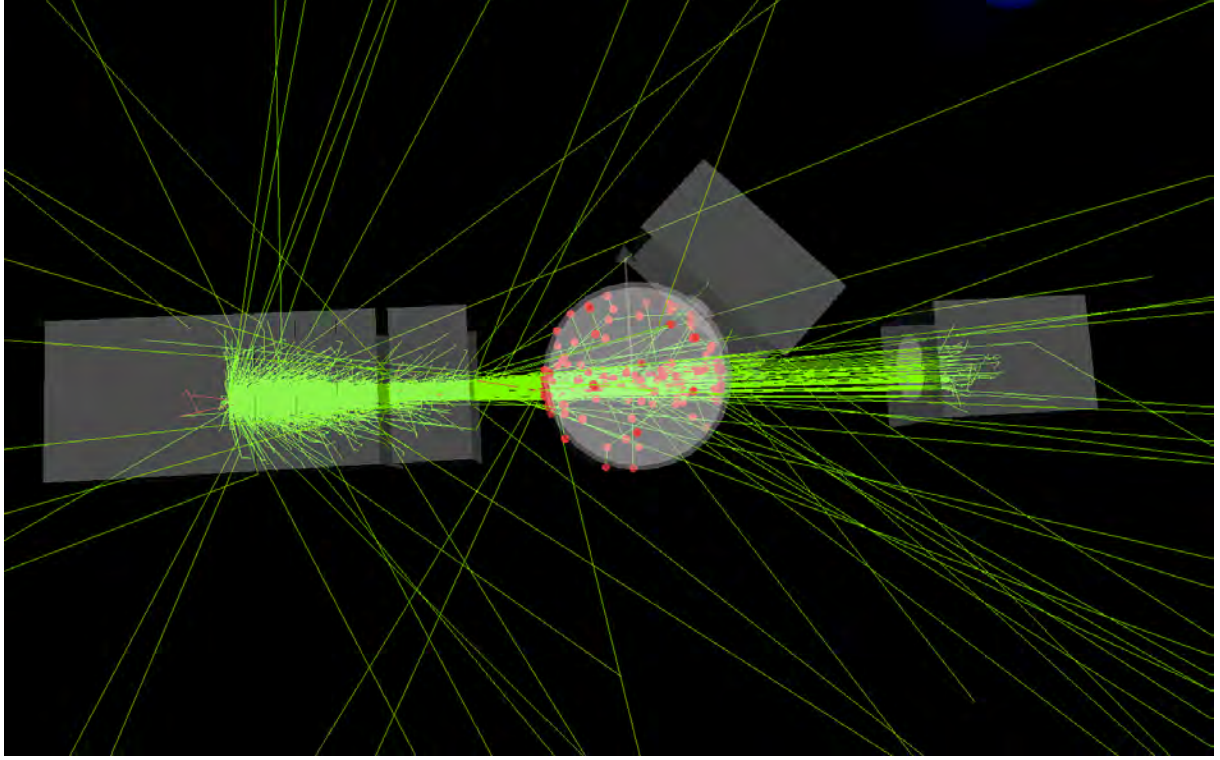


Figure 23: Model of the experiment in Geant4

After performing a large set of these simulations, the optimal dimensions for the collimators were found. The final set of post-scattering collimators is shown in figure 24.

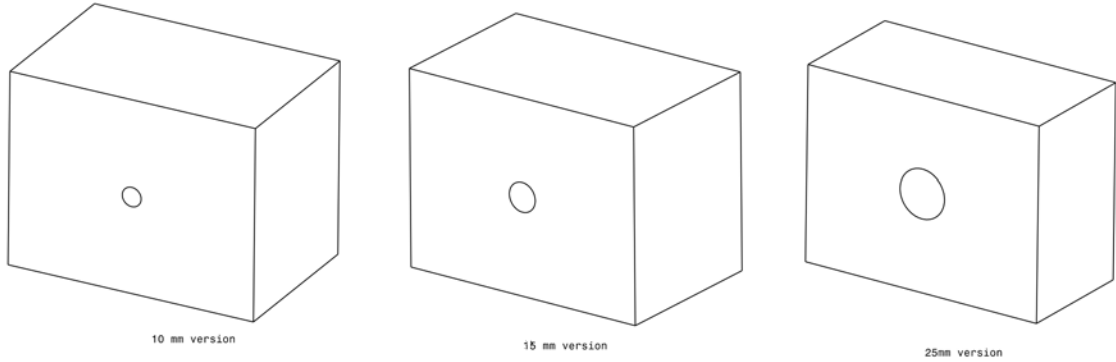


Figure 24: Close shielding blocks

To shield scattering angles from  $20^\circ$  to  $30^\circ$ , a 85 mm long block with a 10 mm hole diameter was used. For scattering angles from  $30^\circ$  to  $60^\circ$  a same-sized block with a hole diameter of 15 mm was used. For angles of  $60^\circ$  and above, a 65 mm thick block with a 25 mm hole was used. Initially, it was planned to have another post-scattering collimator right in front of the HPGe to shield gammas that were randomly scattered outside the LS. As it turned out during Geant4 simulations, the number of “golden” events, i.e., events that only had one interaction in the LS

before being completely absorbed in the HPGe, dropped by 30% due to scattering of gammas on the second post-scattering collimator. Omitting it also saved costs since the source container, collimators, and radiation catcher were all custom made out of lead.

### 2.1.2 Target Cell and Photomultiplier Tube Coupling

The target cell has to hold the liquid scintillator, provide a stable connection between the two PMTs, allow good optical coupling between the cell and the flat surface of the 5" PMTs, and allow bubble-free filling. The range of usable materials was limited by the chemical characteristics of the Gd-doped liquid scintillator. To avoid any uncertainty, only acrylic was used for the cell. Other tested materials that can be in direct contact with the LS without modifying its characteristics are Teflon, some types of Viton, and glass.

The cell (see 3D model in figure 25 and the real cell in figure 26) was made from an optically clear acrylic round tube, two acrylic disks, two O-rings, two rubber gaskets, and two custom-made acrylic screws. The compatibility of the rubber gasket with the LS was not tested, but the design minimizes any direct contact of the LS with it (only through a 3 mm long fine thread in the acrylic). It can hardly be seen from the figures, but the cell's wall thickness is only 3.175 mm. Initially, a cell with 5 mm walls was used, but Geant4 simulations again showed that a thinner wall reduced interactions in the acrylic by 20 %.

The individual parts of the cell were machined and later glued together with acrylic glue (SCI-GRIP 3 Very Fast Set, clear, water-thin, Solvent Cement ACRYLICS) that had also been previously tested for compatibility. The two-screw design allows air to leave the container through one hole as fluid enters via the other. For the filling procedure, a Teflon funnel and a glass pipette in combination with a syringe were used. It took two days to let all of the bubbles accumulate and then remove them with a glass pipette. In the end, one small bubble was left (see figure 27).

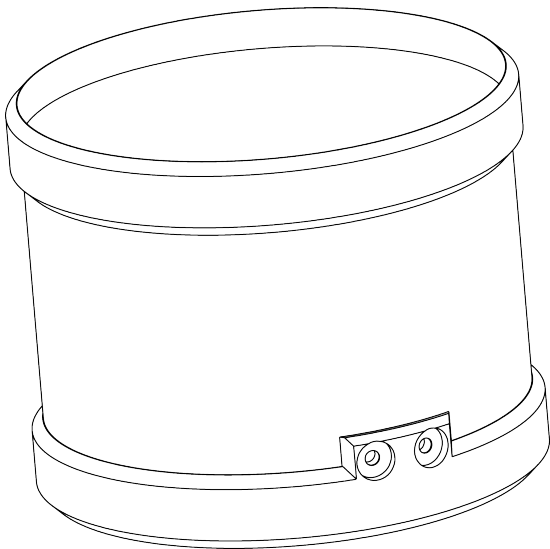


Figure 25: 3D model of the cell



Figure 26: Filled cell

After tests for liquid tightness, the cell was painted with multiple layers of highly reflective white TiO paint (Liquitex Professional HEAVY BODY Acrylic, TITANIUM WHITE) to increase light collection (see figure 28).

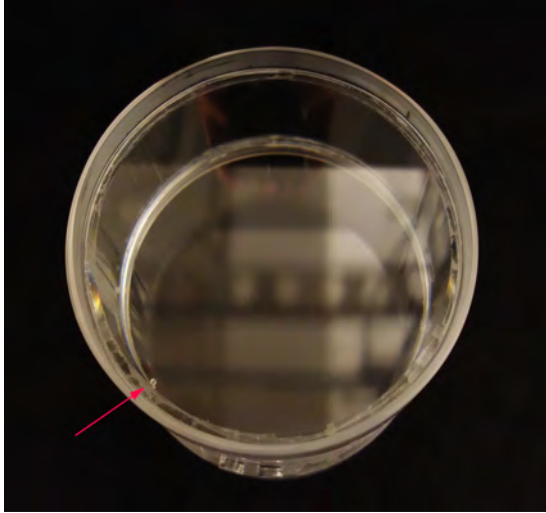


Figure 27: Air bubble in the cell



Figure 28: Cell painted with TiO paint

Both PMTs and the cell were then wrapped with 1" self-fusing tape in an attempt to make them lightproof (figure 29). It turned out later that two layers of this considerably thick tape were not enough to shield all light. Consequently, the full assembly had to be re-wrapped with a layer of aluminum foil as a light barrier.



Figure 29: The completely wrapped assembly

For the optical coupling between the PMTs and the acrylic surface of the cell, optical grease was used (ELJEN TECHNOLOGY, EJ-550 Silicone Optical Grease). The two O-rings at the ends of the cell made the uniform distribution of the optical grease difficult, as the surfaces could only be rotated against each other but not moved in any other way to distribute the grease. Through many rotations of the PMT, a good optical coupling was finally achieved for one side. The exact same procedure was then applied to the other side. Unfortunately, a visual check for a uniform

distribution of the grease was not possible since the other tube was already mounted in position. After installation of the PMT-cell-PMT assembly, it was enclosed in a Tyvek<sup>®</sup> foil to shield the tubes from magnetic fields.

## 2.2 Electronics

The electronic system shown in figure 30 was optimized to be as simple as possible. Attempts were made to keep the number of analog components to a minimum, since each of them has an intrinsic nonlinearity that could negatively affect the measurement.



Figure 30: Electronics rack

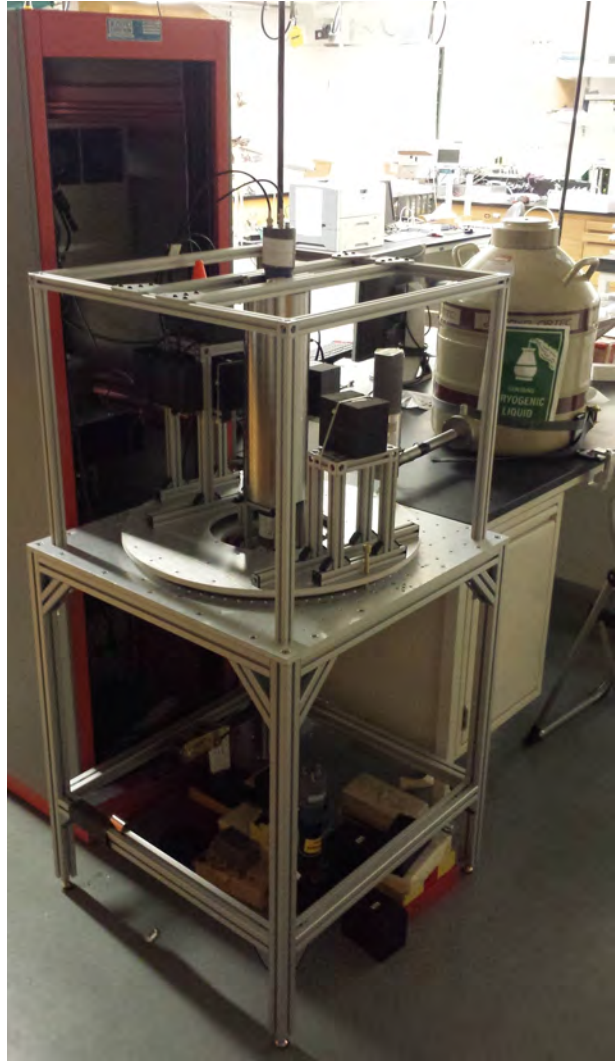


Figure 31: Compton spectrometer

### 2.2.1 Block Diagram and Trigger Description

The block diagram in figure 32 shows all components of the electronics system. It also shows that all trigger decisions are based solely on the signal in the HPGe detector, regardless of whether there was a signal in the PMTs.

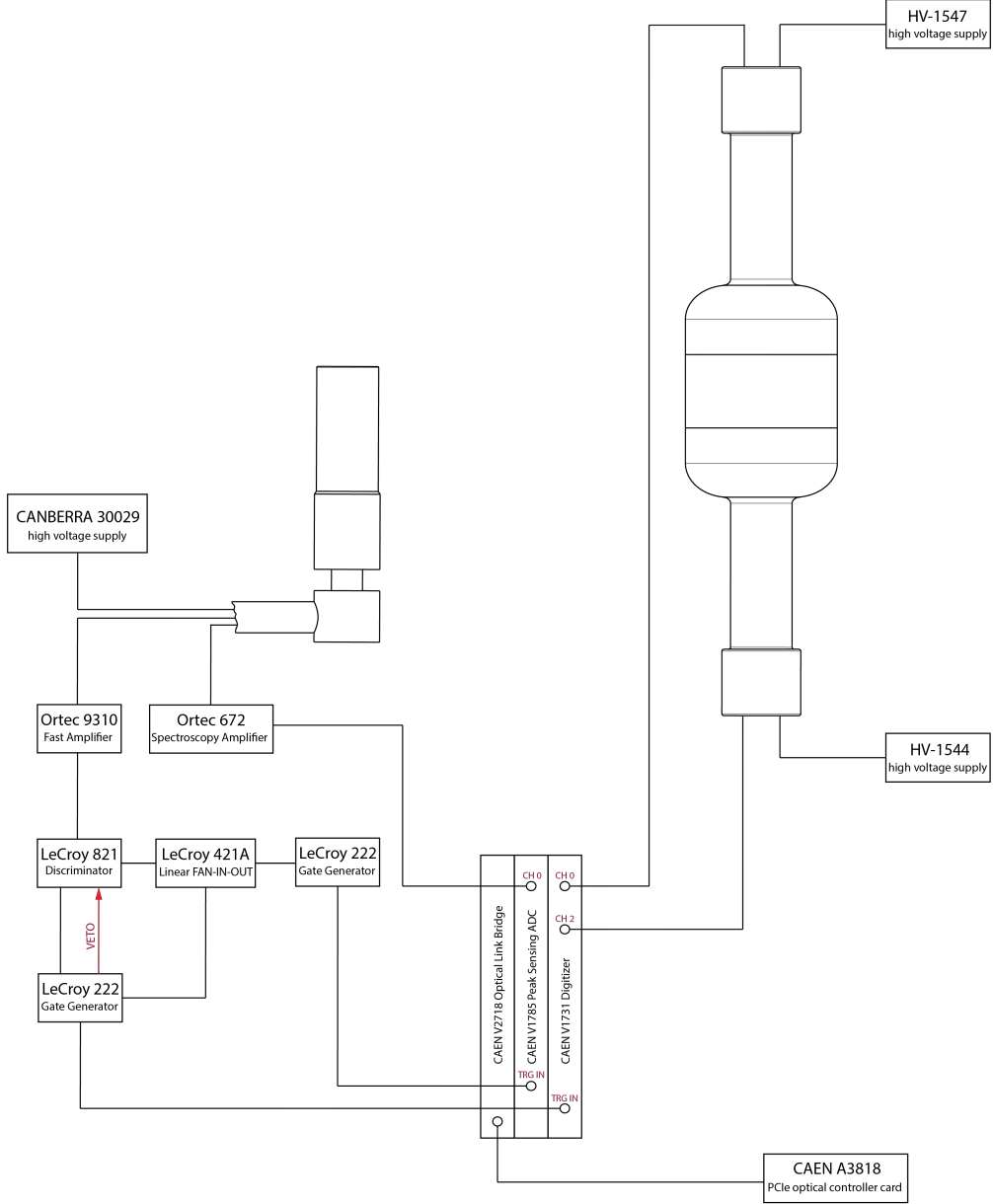


Figure 32: Block circuit diagram

The trigger logic is implemented with NIM modules, while the experimental data is recorded with a CAEN VME system. If an event in the HPGe detector passes the discriminator's threshold, which is equivalent to about 200 keV, it causes a readout to be triggered. Once a trigger is registered in the NIM logic, a 1 ms veto window is opened to keep other events from interfering with the readout. During that time, a copy of the HPGe-detector signal is integrated by a spectroscopy amplifier, which takes about  $4\mu s$ . Meanwhile, within a few hundred ns of the HPGe event, the trigger is received by a CAEN V1731 8 bit, 500 MS/s digitizer, which continuously stores the waveforms of both PMTs in its custom-sized  $1.6\mu s$  circular buffer. After a delay of  $3.6\mu s$ , a CAEN V1785 12 bit peak sensing ADC receives a trigger from the NIM logic, causing it to record the highest value of the integrated peak. Once both cards have processed their inputs and are ready for readout, it takes the data acquisition system (DAQ) about  $24\mu s$  to read out both cards.

The trigger rate was angle-dependent. The highest trigger rate, of about 140 Hz, was observed

at the  $120^\circ$  position. Out of 140 events per second about 35 were PMT singles and 104 were HPGe singles. The remaining event was either an accidental background or an actual coincidence event.

To generate enough PMT-only signals (PMT singles) for later calibration, the second half of the trigger window was used to open a gate for random signals in the PMT system. During that time any event in the LS that passed a threshold equivalent to 50 keV was recorded. The additional logic for this procedure, which is not shown in the block diagram in figure 32, involves a few fan-in-out and gate generators.

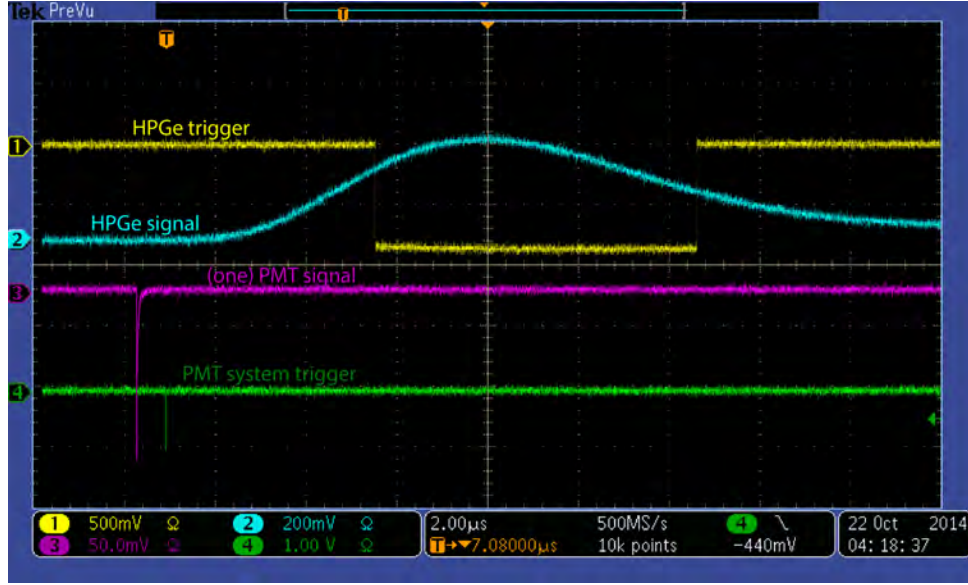


Figure 33: Trigger signals and detector signals: The peak sensing ADC locates the highest point of the HPGe signal (cyan) within the HPGe trigger window (yellow). The digitizer is triggered by the PMT system trigger (green) and saves the waveforms of both PMT tubes (purple).

Figure 33 shows a typical coincidence event on the oscilloscope. The actual trigger from the HPGe detector's trigger signal is not shown but it is located a few hundred ns before the PMT system trigger. The digitizer card is post-triggered meaning that once a trigger is issued to the card it makes the previous  $1.6\mu\text{s}$  available for readout but nothing that follows the trigger. The HPGe trigger gate in figure 33 is perfectly timed with the integrated signal from the spectroscopy amplifier. Here one has to be cautious that the trigger gate is not too small and not bigger than the card allows.

## 2.2.2 Detectors

### HPGe Detector

To meet the challenges of the experiment a sub-percent energy measurement of the scattered gamma is necessary. To this day only HPGe detectors can achieve such a resolution. The detector, an ORTEC High Purity Germanium detector, Model No.: GEM-23185-S, was used in combination with a CANBERRA MODEL 30029 H.V. POWER SUPPLY, which supplied the detector with a bias voltage of +2800V. The detector has an internal pre-amplifier and provides several outputs. The detector was cooled with 30-50 liters of liquid nitrogen per week and grounded to the electronics rack.

## Photomultiplier Tubes

The requirements on the PMTs were to have a high quantum efficiency at the wavelength emitted by the liquid scintillator, and a high gain. Two ET ENTERPRISES Electron Tubes, 130 mm (5") 9330B series photomultiplier tubes with type RB1108 (CS638DSN2-01) voltage dividers were used in the experiment. The high voltage was supplied by a POWER DESIGNS PACIFIC, INC. PALO ALTO CALIFORNIA MODEL HV-1547, High Voltage Regulated DC Power Supply (1-3000V, 40mA), for one tube, and by a POWER DESIGNS PACIFIC, INC. PALO ALTO CALIFORNIA MODEL HV-1544 High Voltage Regulated DC Power Supply (1-3000V, 20mA), for the other tube. The tubes were operated at an initial voltage of about 1200V and later at slightly higher voltages. The operating voltage for both tubes was matched by looking at PMT-only spectra of both tubes. The high voltage was then adjusted so that the two spectra visually overlapped. Any small deviation in gain was corrected during data analysis by multiplying one signal with a weight factor before adding them to the other one.

### 2.2.3 NIM System

The NIM system consists of an ORTEC 9310-16 16 Channel Fast Amplifier, a LeCroy MODEL 821 QUAD DISCRIMINATOR, two LeCroy MODEL 222 DUAL GATE GENERATORS, a LeCroy MODEL 429A LOGIC FAN-IN-OUT, and an ORTEC 672 SPECTROSCOPY AMPLIFIER AND GATED INTEGRATOR. The NIM system without the additional logic for the PMT singles trigger is shown in figure 34.

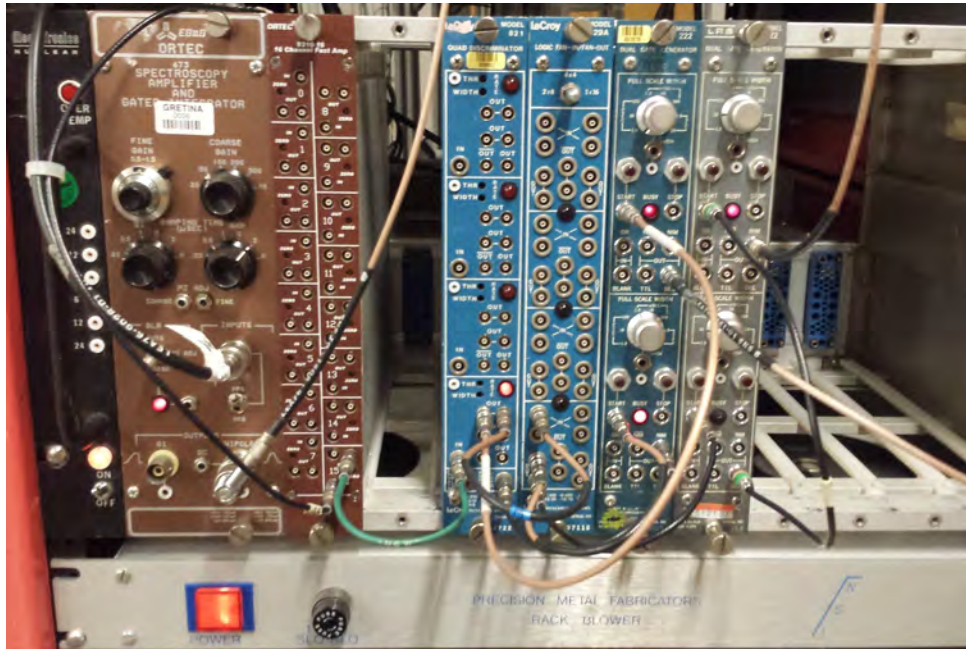


Figure 34: NIM modules make up the trigger logic

### 2.2.4 VME System

The CAEN VME cards used for the experiment are shown in figure 35. The interface to the VME bus is provided by a CAEN A3818 PCI Express x8 CONET2 Controller in combination with a CAEN V2718 VME-PCI Optical Link Bridge. The data transfer rate of this combination allows up to 85 MB/sec which is much greater than that needed for the experiment. The communication between the DAQ software and the VME system was based on the lowest level library provided

by CAEN, CAENVMELib. With hindsight on the programming effort, it would have been easier to use the higher level CAENComm library, or even a combination of CAENComm library and the even higher level CAENDigitizer library. However this last approach has some disadvantages: Two handles, one for each card, are needed, which restricts the modular design of the software; timing in setting the cards online might have also become an issue. Fortunately the additional programming effort led to a better understanding of how the CAEN cards and the VME bus work.

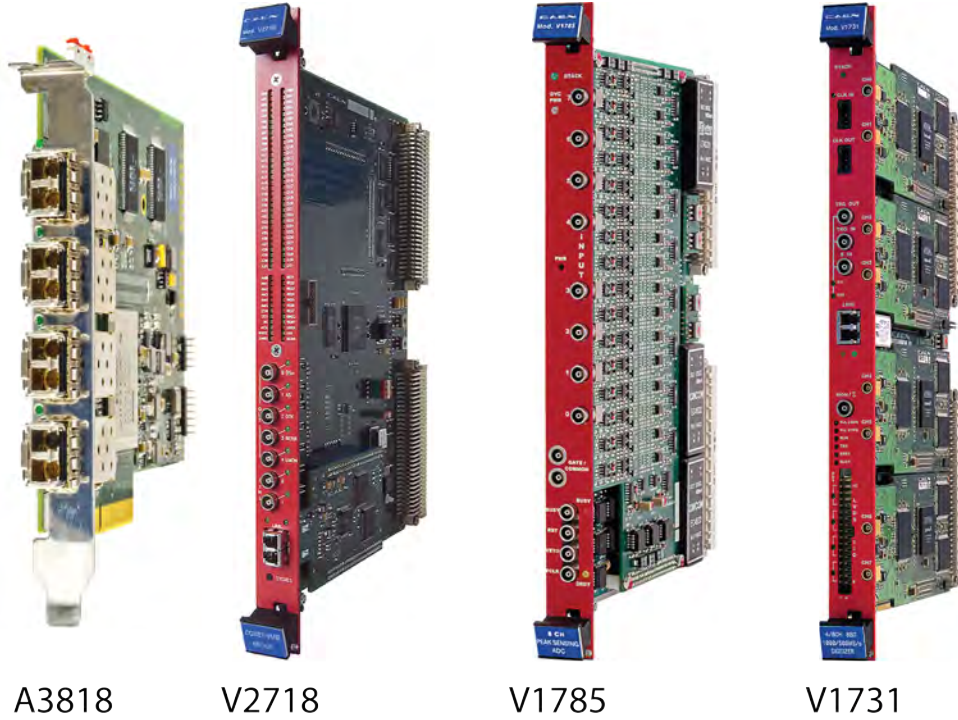


Figure 35: CAEN VME cards used in the experiment

The CAEN V1785 8 Ch Dual Range Multievent Peak Sensing ADC is used to find the peak provided by the ORTEC 672 SPECTROSCOPY AMPLIFIER AND GATED INTEGRATOR within the provided trigger gate. The V1785 has a 12 bit resolution over two selectable ranges from 0 to 4 or 0 to 0.5 V. If a trigger signal is issued to the card's TRG IN, the event is saved to the buffer. The card can store up to 32 events in its buffer, which are then read out by the VME controller card. The conversion time is  $2.8\mu\text{s}$  per channel, which is far less than the available time (veto) of about 1 ms.

The CAEN V1731 4/8 Ch. 8 bit 1000/500 MS/s digitizer uses a circular buffer to constantly record waveform data from the PMTs. Once it gets a trigger signal, these waveforms are made available for readout. The card's buffer can hold up to 2 MS/ch at a sampling rate of 500 MS/s, which corresponds to 4 ms. If the 4 ms buffer is full, the card can go on to another memory block from the individually assignable buffer. The card can be used to define custom events with a specific recording length before and after the trigger. In this experiment the total waveform recorded was scaled-down to  $1.6\mu\text{s}$  of pre-trigger samples, with no post trigger samples.

## 2.3 Data Acquisition Software

For the readout of the VME cards, a stand-alone data acquisition system (DAQ) was programmed in C++. The DAQ consists of several classes which handle different tasks. The general layout

is shown in figure 36. The black lines show to which class each object belongs with respect of memory management; the green lines show how references to classes are passed around; and the red lines represent the path data takes from the VME system to the ROOT file where it is stored.

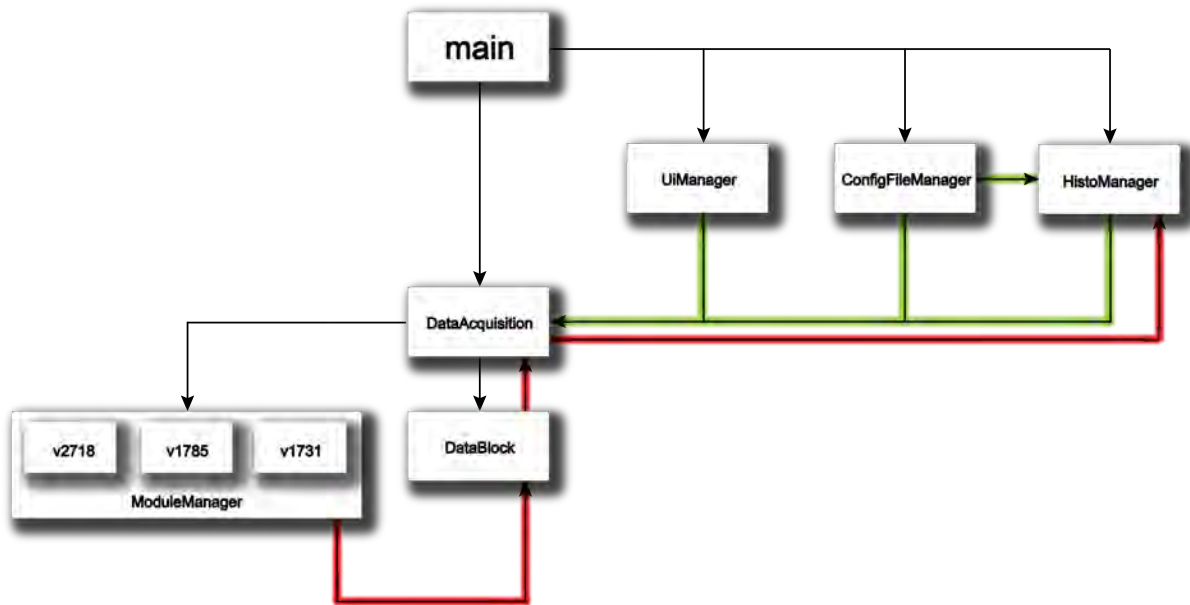


Figure 36: Block diagram of the DAQ program

The DAQ has been tested extensively and has proven to be able to handle event rates of a few kHz, which is more than sufficient for the experiment, with rates around 100 Hz.

### 3 Data Analysis

This section walks over the complete data analysis procedure. Analysis was implemented in Python, utilizing ROOT classes. During the first stage of analysis, any instability or nonlinearity in the detectors and/or the readout electronics is determined. The methods to do this are summarized in section 3.2.

#### 3.1 Acquired Data

Each run consists of a scan over 14 different angle positions from  $20^\circ$  to  $120^\circ$ . A  $5^\circ$  separation is used from  $20^\circ$  to  $50^\circ$ , while at higher angles a  $10^\circ$  spacing is used to avoid gaps in the electron energy. The data taking time per angle is about one day with the 2.59 MBq  $^{60}\text{Co}$  source. Data can be collected in less time, but this time spacing is convenient and guarantees good statistics. The trigger rate is angle dependent and ranges from  $\sim 50$  Hz at  $20^\circ$  to  $\sim 140$  Hz at  $120^\circ$ . The unexpected lower trigger rates at shallow angles can be explained by the small hole size of the close shielding blocks at small angles. Only about 0.1% of all events at the  $20^\circ$  position are coincidence events in the considered 1.33 MeV region. The remaining events are made up by  $\sim 25$  % PMT singles (HPGe signal zero or negligible),  $\sim 74$  % HPGe singles (PMT signal zero or negligible), and  $\sim 1$  % random background events including the events in which the gamma is not fully absorbed by the HPGe detector. At the  $120^\circ$  position the percentage of coincidence events goes down to 0.03 %.

#### 3.2 Data Processing

##### 3.2.1 HPGe Detector Stability

The 3% drift in HPGe detector signal that happened over a period of two days in the beginning of the measurements underlines the importance of data validation. Figure 37 shows the movement of the Tl-208 peak ( $E_\gamma = 2614.5$  keV) that was observed. The drift stretched over a range of 50 ADC values, which is equivalent to 80 keV.

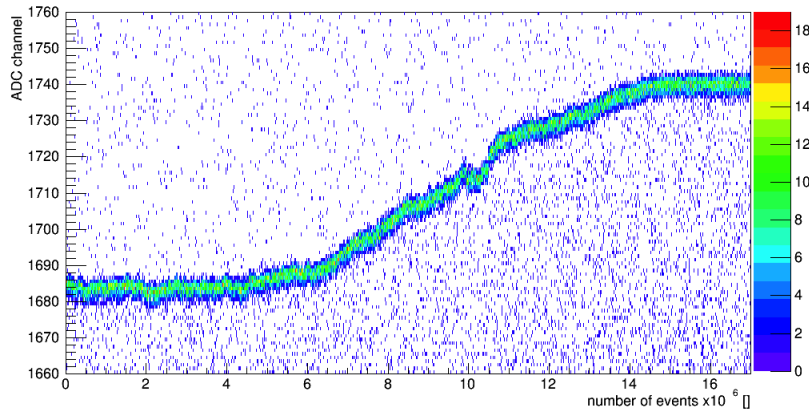


Figure 37: Observed drift in HPGe detector signal

While smaller drifts have occurred, such a big drift has never been observed in the experiment since. The cause of the shift is not yet fully understood. There are two analog components in the HPGe system that could have played a part: the internal pre-amplifier, and the external gated integrator ORTEC 672. The first time the system became unstable was after the settings of the integrator were changed. The signal did not return to its baseline until the settings of the integrator were repeatedly changed before returning them to the desired values. This behavior

points to a knob or selection wheel of the external integrator as the source of the error. To prevent drifts, the integrator is not touched during data taking and re-calibrated after changes have been made to it. During later runs the observed drifts were below 0.2 %.

Each data file is checked for detector stability before being used in the analysis. The stability of the HPGe detector and its readout chain is monitored by looking at the relative movement of the  $^{214}\text{Bi}$  (609.31 keV / channel 481) and the  $^{208}\text{Tl}$  (2614.51 keV / channel 1740) peak positions. The system was highly stable with drifts well below 0.2 % for all files for the later data analysis. Figure 38 and 39 show the peak drift percentage of data bins relative to the true energy of that peak. Each bin is an average over 200.000 events.

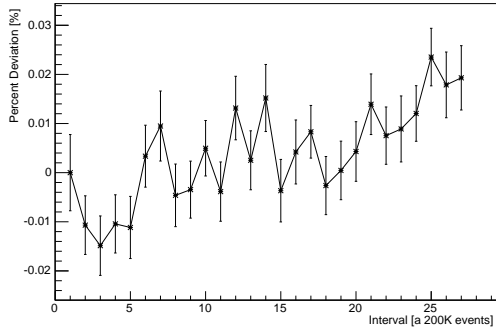


Figure 38: Fluctuations in the  $^{208}\text{Tl}$  peak

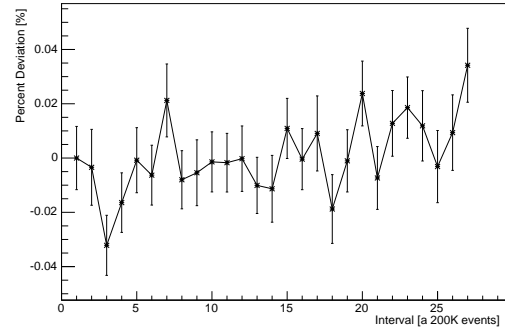


Figure 39: Fluctuation in the  $^{214}\text{Bi}$  peak

The maximum absolute movement of both peaks for all files in the analysis is shown in table 40.

Position [deg]	$^{208}\text{Tl}$ deviation [%]	$^{214}\text{Bi}$ deviation [%]
20	0.0161	0.0241
25	0.0107	0.0257
30	0.0195	0.0369
35	0.0186	0.0310
40	0.0227	0.0591
45	0.0343	0.0558
50	0.0248	0.0368
60	0.0235	0.0342
70	0.0309	0.0380
80	0.0293	0.0232
90	0.0280	0.0561
100	0.0229	0.0500
110	0.0253	0.1628
120	0.0296	0.1353

Figure 40: Maximum absolute peak fluctuations for each data file used in the analysis.

### 3.2.2 HPGe Detector Calibration

After the data was checked for drifts, the conversion function between ADC counts and energy is determined. This is done for each data file to counteract slow drifts over a whole data set. A typical HPGe detector spectrum from the first test runs is shown in figure 41. It shows two

dominant  $^{60}\text{Co}$  peaks at ADC values 835 (1173.23keV) and 935 (1332.5keV) caused by direct source gammas. Attempts to eliminate these made at a later stage turned out to be too much of an effort with respect to their benefit for the analysis.

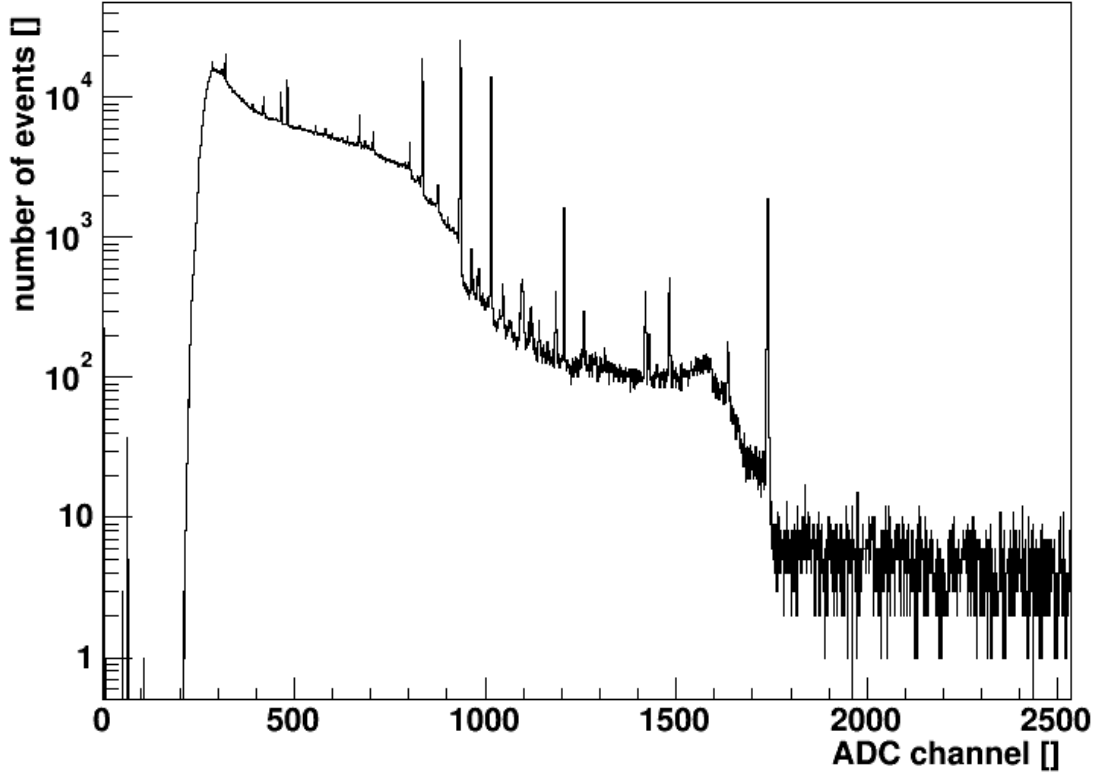


Figure 41: HPGe detector number of events over ADC channel

Calibration is implemented by identifying background radiation peaks of known energy in the measured spectrum. Some widely used background radiation peaks are listed in figure 2. A comparison of measured and known values allowed finding a quadratic conversion function.

This procedure is automated in a script which uses ROOT's TSpectrum class to find the peaks and estimate the background. The step by step calibration procedure:

1. The histogram is searched for peaks: The peak finding algorithm considers all peaks above a specified threshold and returns their positions as well as number of peaks found. All peaks shown in figure 42 that were found by the software are marked with a red triangle on top. The minimum number of peaks for a quadratic fit is 3, although the minimum number of peaks the software required was set to be 5; otherwise, the procedure fails.
2. For easier fitting, the background is estimated and subtracted from the signal. This way it is possible to fit the peaks with simple Gaussian functions. The background is estimated by ROOT's TSpectrum class and is indicated by the red line in figure 42. The result of the background subtraction is shown in figure 43.

Element	Energy [keV]	Common intensity []	Element	Energy [keV]	Common intensity []
U-235	185.72	57.2	Ac-228	968.97	15.8
Pb-212	238.63	43.6	Pa-234m	1001.03	1.021
Ra-223	269.49	13.7	Bi-214	1120.29	14.907
Pb-214	295.22	18.5	Bi-214	1155.19	1.635
Ac-228	338.32	11.27	Co-60	1173.23	99.85
Pb-214	351.93	35.6	Bi-214	1238.11	5.827
Ac-228	409.46	1.92	Co-60	1332.49	99.98
Ac-228	463	4.4	Bi-214	1377.67	3.967
Tl-208	583.19	30.6	Bi-214	1407.98	2.389
Bi-214	609.31	45.49	K-40	1460.82	10.66
Cs-137	661.66	84.99	Ac-228	1588.2	3.22
Bi-212	727.33	6.74	Bi-212	1620.74	1.51
Bi-214	768.36	4.891	Ac-228	1630.63	1.51
Ac-228	794.95	4.25	Bi-214	1729.6	2.843
Bi-214	806.17	1.262	Bi-214	1764.49	15.28
Tl-208	860.56	4.48	Bi-214	1847.42	2.023
Ac-228	911.2	25.8	Bi-214	2204.21	4.913
Bi-214	934.06	3.096	Tl-208	2614.51	35.85

Table 2: Commonly used reference peaks for gamma detector energy calibration

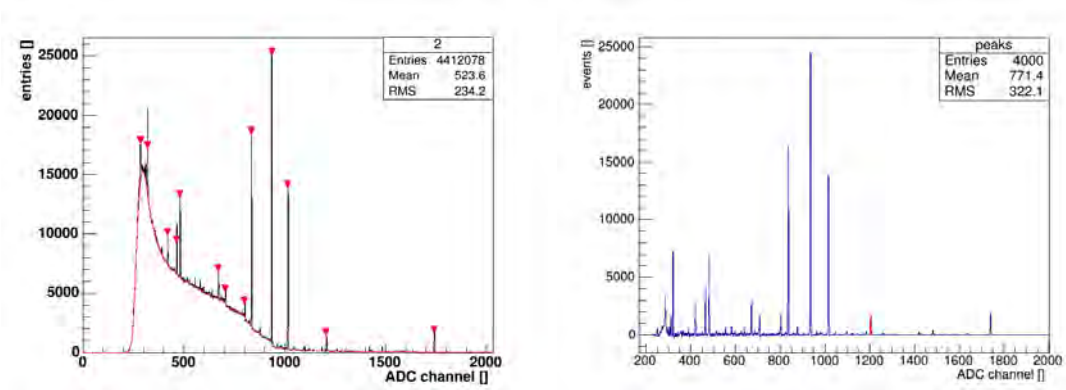


Figure 42: Peaks and background found by ROOT's TSpectrum class

Figure 43: Spectrum after background subtraction

3. Identified peaks are fitted with Gaussian functions and the mean value plus the statistical error of the fit are recorded.
4. The ADC values of the fitted peaks are then compared to an internal database in which the anticipated ADC values and energies of these peaks are saved. If one of the fitted peak's ADC values falls within a 3 ADC window of a saved one, it is considered a hit and recorded into an array. Peaks that do not fall within that window are discarded.
5. Using Python's SCIPY package, a least-squares fit, of the quadratic fitting functions and the values in the array, is made to obtain the function's (equation (25)) coefficients.

$$E = a + b \cdot ADC + c \cdot ADC^2 \quad (25)$$

6. The function is then checked for compliance by calculating the absolute deviation of data points from it. If any of the data points shows an absolute deviation of more than 1 keV, the fit is discarded because of a lack of accuracy.

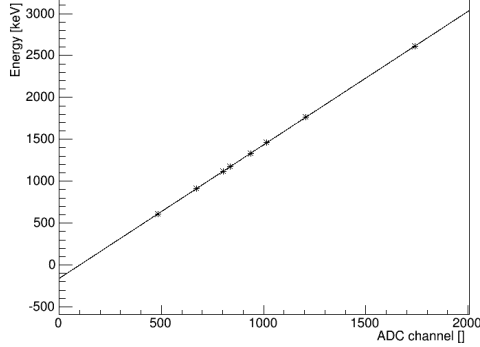


Figure 44: (Quadratic) fit function

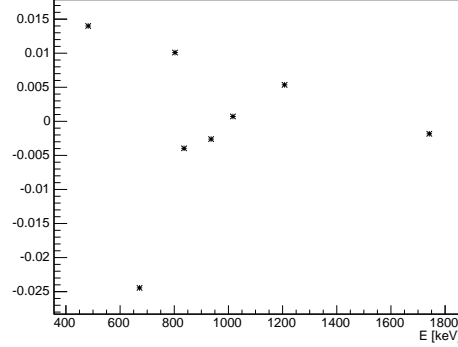


Figure 45: Absolute offsets of known peaks from the conversion function

7. The obtained function parameters and the error are returned as a list to the calling function.

**Error:** The error from the HPGe system is estimated by calculating the root mean square (RMS) that the energy offset's known peaks have from the conversion function. Figure 45 (60° position file) points out that there is no notable divergence of the ADC-mean peak position pairs from zero. The calculated RMS includes drifts and the nonlinearity of the system. Consequently the RMS of these data points is used as an error estimation for the whole HPGe system. The HPGe error in percent of the signal is listed as ' $\sigma_{HPGe}$ ' in table 69. Table 46 shows the constants, the number of peaks found, and the calculated RMS for all files in the scan. Through using a quadratic instead of a linear conversion function, the RMS goes down by a factor of 2 or more. This suggests a small nonlinearity in the HPGe detector system.

Position [deg]	a [keV]	b [ $\frac{keV}{ADC}$ ]	c [ $\frac{keV}{ADC^2}$ ]	RMS [keV]	Peaks found [ ]
20	-159.764	1.596	-1.396e-06	0.065	12
25	-159.807	1.596	-1.428e-06	0.051	12
30	-159.697	1.595	-1.181e-06	0.067	12
35	-159.669	1.595	-1.059e-06	0.054	14
40	-159.801	1.596	-1.343e-06	0.058	13
45	-159.816	1.597	-1.356e-06	0.055	13
50	-159.755	1.596	-1.290e-06	0.050	12
60	-159.664	1.595	-1.428e-06	0.103	14
70	-160.037	1.596	-1.362e-06	0.083	13
80	-159.826	1.596	-1.341e-06	0.086	12
90	-159.630	1.596	-1.267e-06	0.070	10
100	-159.585	1.596	-1.322e-06	0.049	8
110	-158.139	1.593	1.007e-06	0.021	9
120	-158.664	1.594	2.852e-07	0.012	6

Figure 46: Calibration factors for different data files. 'Peaks found' denotes the number of peaks that were found by the calibration script.

Table 46 shows that the number of identified peaks decreases for higher scattering angles. This is caused by direct gammas from the source that lead to two very prominent peaks in the spectrum.

The peak sensing software identifies the individual peaks and discriminates those below a certain fraction of the most prominent one. With the decrease of shielding at higher angles, the source peaks become very prominent and consequently more peaks with low intensity are discarded. The decrease of shielding can be explained geometrically: At low scattering angles a large amount of lead (source collimators and post-scattering collimator) covers the source pellet, but at high angles the shielding of the pellet is only about 10 cm of lead (wall thickness of the source container plus lead blocks at the side of the source). Evidently, the reduced number of peaks does not impact the accuracy of the fit. The fluctuations of the constant 'a' of up to 1.7 keV show that there are slow drifts in the signal, but do not affect the accuracy of the calibration nor of the obtained signal.

### 3.2.3 PMT Charge Integration

The PMT waveforms are recorded by a 500 MS/s, 8 bit CAEN V1731 digitizer card. The upper PMT (PMT0) and the lower PMT (PMT2) are connected to channel 0 and 2 of the digitizer, respectively. Each channel is continuously read into a circular  $1.6\mu s$  buffer. When the card is triggered by an external trigger coming from the NIM system, the buffers are opened for readout. The typical waveforms for an event are shown in figures 47 and 48. The maximum waveform peak size is about 20-30% of the digitizer's dynamic range (1 V) to leave enough room for measurements with higher gain. The signal and the pedestal value are pre-calculated in the DAQ software to make quick checks easier, but the actual value for analysis is calculated with different time windows.

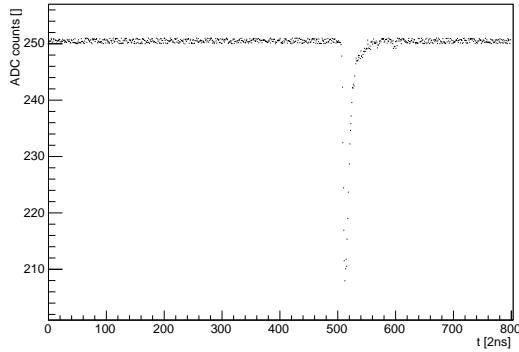


Figure 47: Signal in PMT0

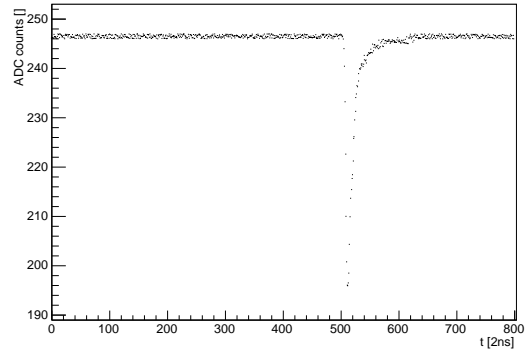


Figure 48: Same signal in PMT2

Figures 47 and 48 reveal slightly different peak heights caused by unequal gains in the PMTs. One of waveforms is later multiplied by weighting factor to account for this inequality before the two signals are summed, to give one total signal representative of the total light output. In order to calculate the signal, one first needs to define an integration window. The integration windows were 400 ns for both the signal and the pedestal. The integration is illustrated in figure 49. The values in the array are simply summed for the two intervals. The grey pedestal region and the red signal region are then subtracted to give the value of the signal.

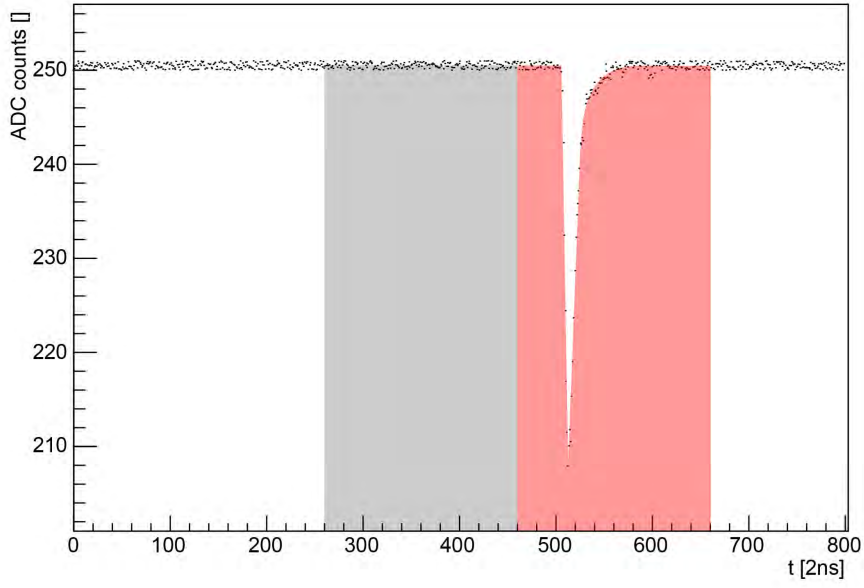


Figure 49: HPGe detector number of events over ADC channel

The biggest trouble with the available digitizer is its low resolution of 8 bits, which causes channel hopping. Channel hopping is the random switching, introduced by external noise, between two different channels of the digitizer. It occurs when the signal's baseline voltage is very close to two adjacent channels. Sometimes it causes the average mean signal in the pedestal window to be a little higher or a little lower than the one in the signal window. Multiplied by the window width, that gives (in the worst case) a  $\pm 400 \text{ ADC} \cdot ns$  bias value for the integrated peak. Channel hopping can be prevented by carefully placing the baseline of the signal in the middle of a channel. This is done by slightly changing the voltage offset of each channel in the DAQ while looking at the pedestal distribution. After final adjustment, the average pedestal signal has one characteristic peak, with some noise lower in value. The pedestal distributions for PMT0 and PMT2 are shown in figure 50 and 51.

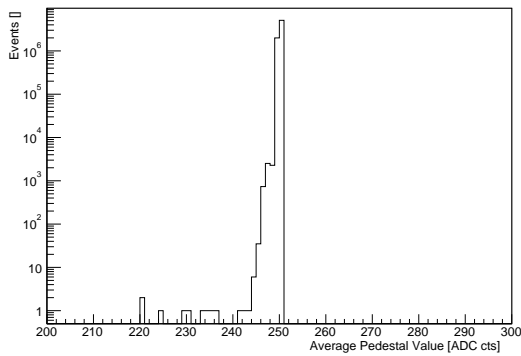


Figure 50: Pedestal value for CH0

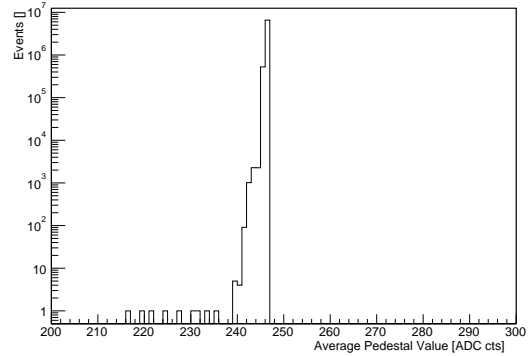


Figure 51: Pedestal value for CH2

Pedestal values that can be found in the far left side of the peak are random events that have happened in the pedestal window. Less energetic events are the reason for the peak's tail towards the left.

### 3.2.4 PMT Gain Stability

The gain of photomultiplier tubes cannot be expected to be stable. PMTs drift for various reasons: Very small changes in high voltage can cause dramatic changes in gain, as do light leaks, temperature changes, and many other effects. Like the HPGe detector, the PMT system also had a major instability during test runs. Shown in figure 53 are 'PMT singles' that are, as explained in section 2.2.1, random events in the LS that are solely collected for calibration purposes. These events form a Compton edge that is characterized by the maximum energy deposited inside the LS cell by gammas from the source. Figure 52 shows the integration of figure 53 along the x-axis, with the Compton edge around an x-value of 700. Figure 53 shows large movements of the peak and the whole spectrum. It is obvious that such movements seriously bias any result.

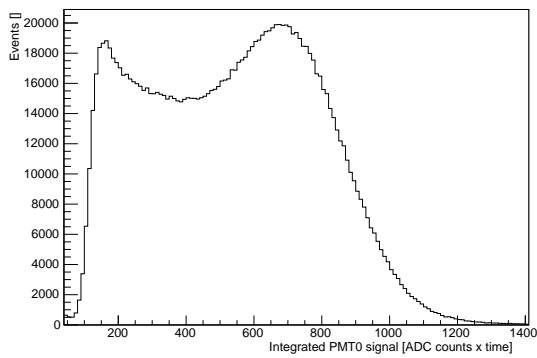


Figure 52: Projection of singles spectrum

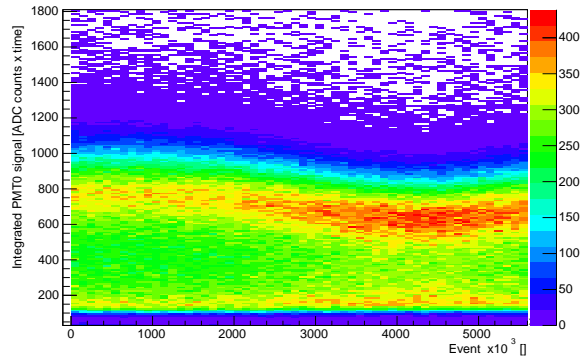


Figure 53: Drift in the PMT0

The drift was caused by a tiny light leak in the black tape of the tube wrapping. As soon as the light in the room was switched on, many photons penetrated the wrapping and got into the cell and into the PMT (mainly the upper one). This constant bombardment of photons caused the PMT to draw more current from the power supply which in turn lowered the high voltage output and consequently the gain. The issue was finally resolved by re-wrapping the cell and the tubes, but this time with an additional layer of aluminum foil. Figure 54 illustrates the stability of the spectrum after re-wrapping.

During data analysis the gain stability of each PMT is measured by comparing intervals of  $10^5$  PMT single events throughout a run to a reference interval. Gain drifts of up to 2% between the intervals were observed. In order to address these drifts, individual intervals are scaled by a scaling factor that gives the best consistence when compared to the reference interval with a Kolmogorov-Smirnov test. The Kolmogorov-Smirnov test is necessary in this case since fitting the Compton peaks results in fitting errors on the order of a few percent. The PMT0 singles spectrum of the  $60^\circ$  data file and its scaling factors are shown in figure 54 and 55.

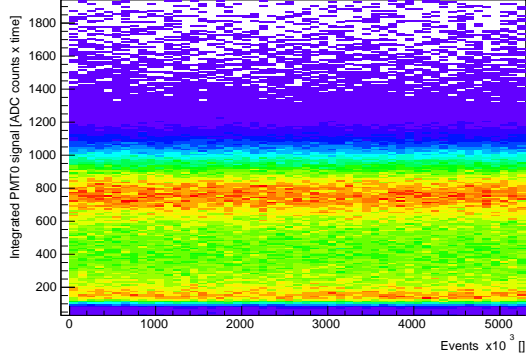


Figure 54: PMT0 singles of the 60° position

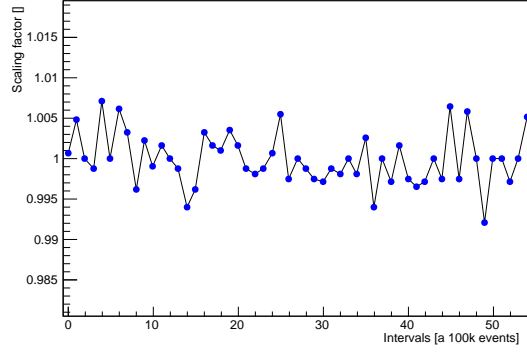


Figure 55: Scaling factors for PMT0

The scaling factors are found for each channel individually before being applied. To address slow drifts in gain over the whole data taking period, the individual spectra of each data file are scaled against a reference file by the same method. After both channels are equalized among all runs, one channel is multiplied by a weight factor before both signals are summed. The weight factor is the same for all files since all the spectra were equalized in the previous process. The sum is later divided by a constant factor of two to make the relative signal consistent with the electron energy. Figure 56 shows the normalized spectra of PMT0 for all runs. The summed spectra after the scaling process are shown in figure 57.

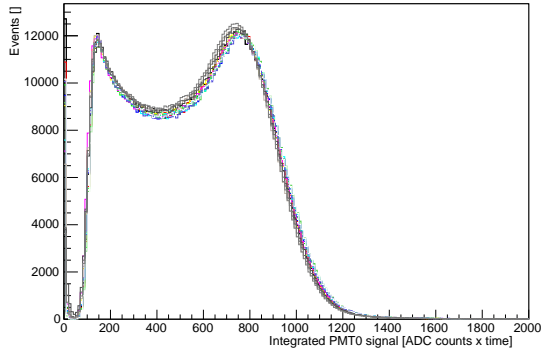


Figure 56: Unscaled PMT0 singles spectra

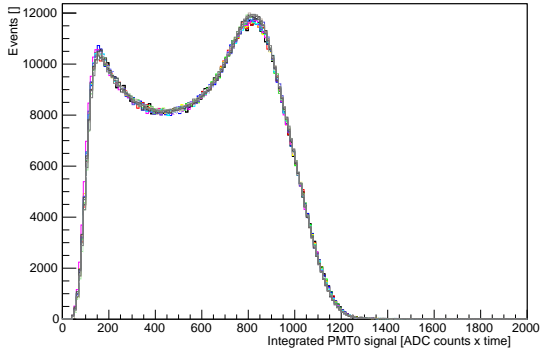


Figure 57: Scaled PMT0 single spectra

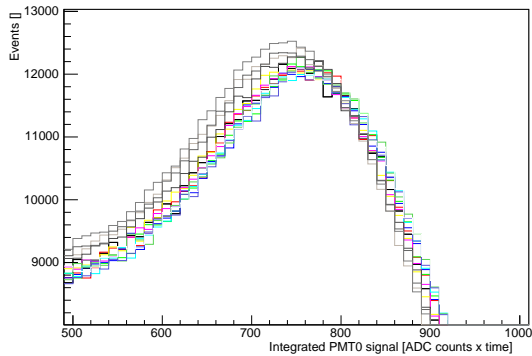


Figure 58: Zoomed Peak figure 56

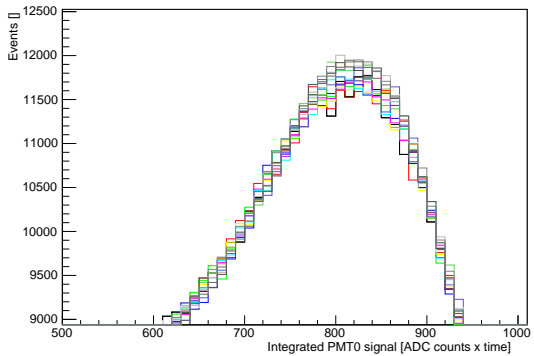


Figure 59: Zoomed Peak figure 57

**Error:** The precision of the calibration can be estimated by looking at the KS-test distribution. The average  $1\sigma$ -width of all intervals is chosen as the calibration uncertainty. For more

information, please see section 4.

### 3.3 Nonlinearity Analysis

With the conversion function's parameters found (section 3.2.2), the HPGe events are converted from ADC values to  $E_{HPGe}$ , the energy in keV measured by the HPGe detector. Simultaneously, the PMT stability correction and the summing of the individual PMTs (as described in 3.2.4) is done, leading to  $E_{vis}$ , which is equivalent to the light produced in the LS. Figure 60 shows light output  $E_{vis}$  over  $E_{HPGe}$  for the  $60^\circ$  position.

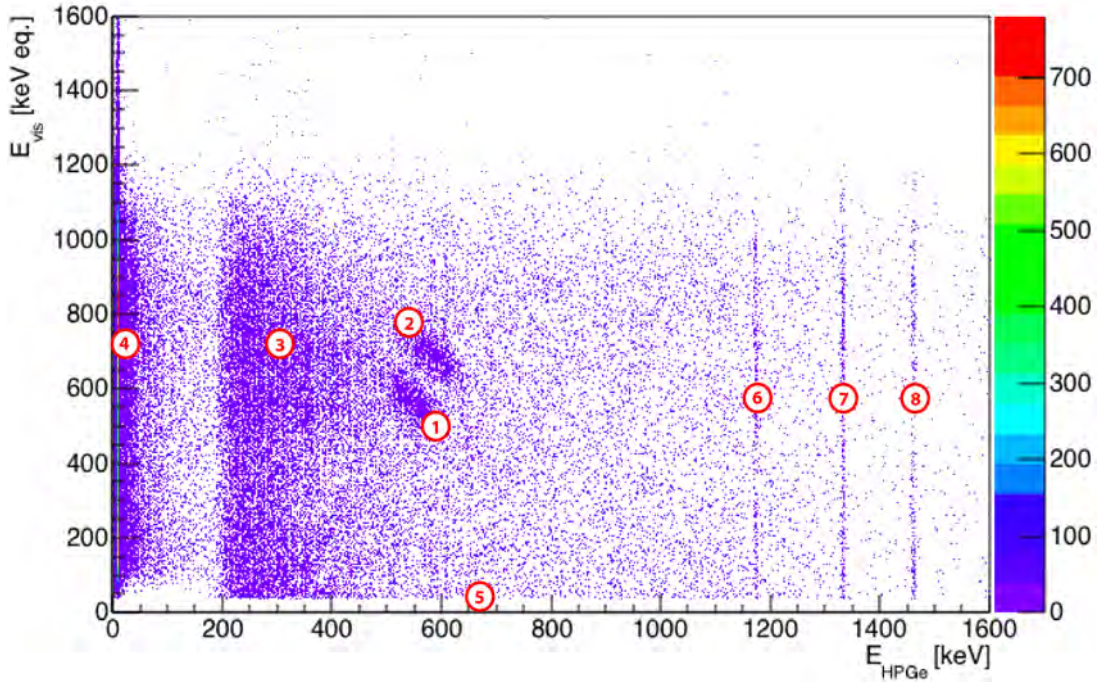


Figure 60: Experimental data for the  $60^\circ$  position. The narrow white line along the x-axis holding no events is caused by the data processing, where events with no or a small signal in the PMTs were filtered out.

The numbers in figure 60 denote different event types:

- Since  $^{60}\text{Co}$  decays by double  $\gamma$ -decay, there are two coincidence regions, ① for the 1173.2 and ② for the 1332.5 keV  $\gamma$ .
- Region ③ contains events during which the  $\gamma$  was not fully absorbed in the HPGe detector (Compton region).
- The PMT singles used for PMT calibration in region ④ can be seen, while HPGe singles were removed from the data ⑤ to keep the files manageable.
- Direct gamma events from the source ⑥, ⑦, and prominent  $^{40}\text{K}$  background radiation ⑧ show up as constant HPGe detector energy lines.

The spread in  $E_{HPGe}$  is caused by geometry effects. Figure 21 shows that the scattering can take place anywhere within the solid red area leading to a smearing of the actual scattering angle and therefore a spread in  $E_{HPGe}$ . The spread in  $E_{vis}$  is caused by the resolution of the LS which is

about 2 % at 1 MeV. With this plot, the relative nonlinearity is already evident when plotting  $E_{vis}/E_e$  over the electron's energy  $E_e = E_{\gamma_i} - E_{HPGe}$  for different angles/electron energies, as shown in figure 61 - figure 64.

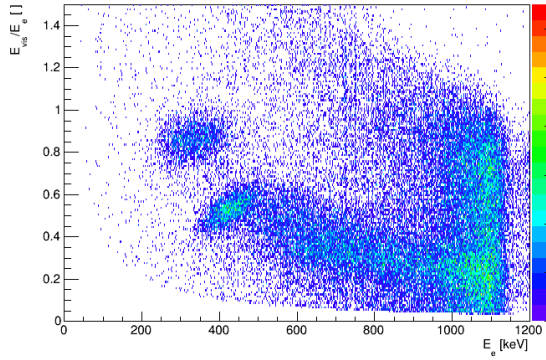


Figure 61: 30° position

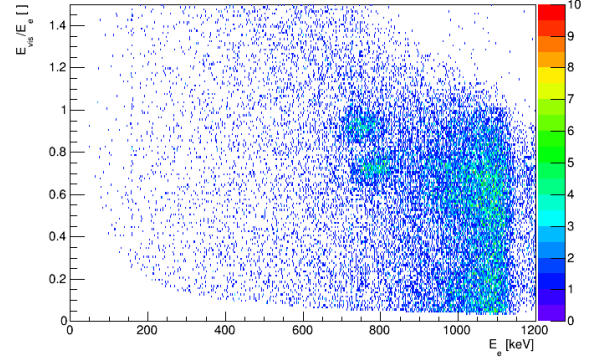


Figure 62: 60° position

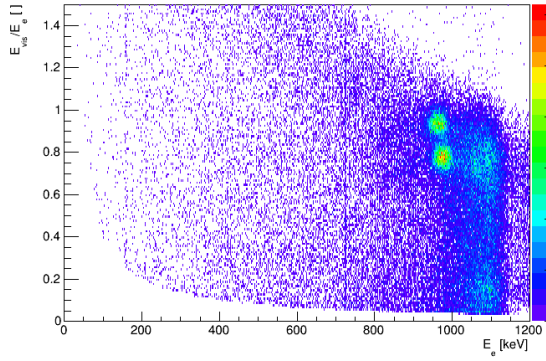


Figure 63: 90° position

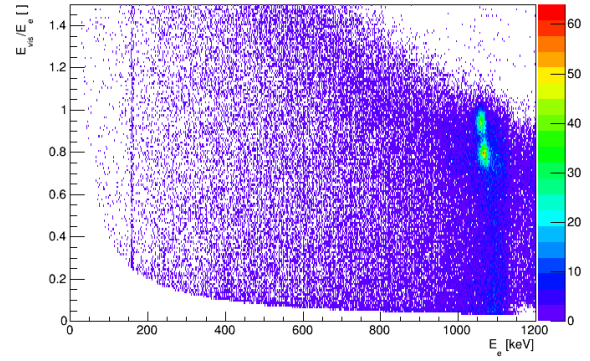


Figure 64: 120° position

The coincidence region of interest is the upper one (1332.5 keV gamma). The lower coincidence region cannot be used in this method since the divisor has the wrong energy and therefore biases it. In addition, the lower energy coincidence region is also biased by events where the gamma did not get fully absorbed in the HPGe detector (Compton events). Figures 61 to 64 show that the higher the electron energy, the closer the two coincidence regions get. At angles higher than 60°, the regions start to bias each other, as we will see soon.

To extract the nonlinearity, the coincidence regions for each file are sliced into short intervals along the  $x/E_e$ -axis and projected towards the y-axis. A selection of these projections, one per scatter plot above, is presented in figures 65 to 68.

While the two peaks are very well separated for the positions up to 50°, they start to overlap at higher electron energies (figure 66 to 68). There are two approaches to deal with this: One is to find a custom fit function that includes the background and fits both peaks. Due to the variety of different shapes for each slice, finding an appropriate fitting function that converges in all cases is difficult. In the applied alternative approach, a simple Gaussian is used to fit the second peak throughout the data. The bias of this method is estimated with MC data and is further discussed in section 4.4.

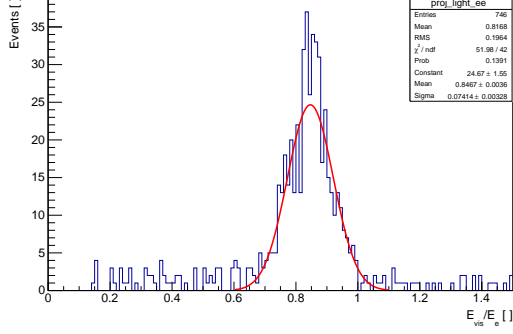


Figure 65: 30° projection, 275-305 keV slice

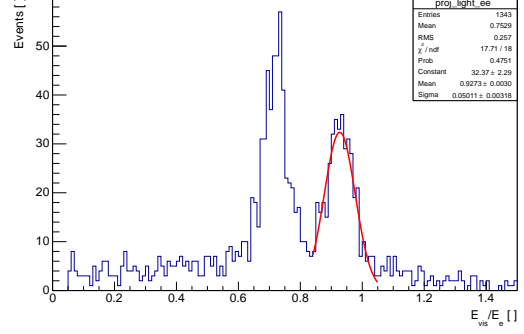


Figure 66: 60° projection, 760-790 keV slice

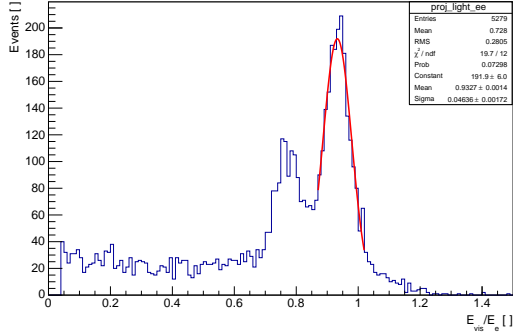


Figure 67: 90° position, 930-960 keV slice

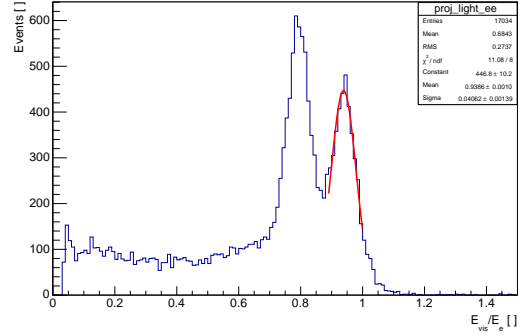


Figure 68: 120° position, 1050-1080 keV slice

### 3.4 Error Propagation

Linear error propagation is used throughout the analysis. The propagation of systematic errors in relative nonlinearity,  $N_L = E_{vis}/E_e$ , caused by the detectors and the electronics chain can be estimated by:

$$\sigma_{N_L(sig.)} = \sqrt{\left(\frac{1}{E_e}\right)^2 \cdot dE_{vis}^2 + \left(\frac{E_{vis}}{E_e^2}\right)^2 \cdot dE_e^2} \quad (26)$$

The individual parts of the electron energy  $E_e = E_{\gamma_i} - E_{HPGe}$  had a very small error and were therefore not treated separately. The bias of the fitting procedure, introduced by multiple scattering and the low energy peak, is considered by adding it to  $\sigma_{N_L(sig.)}$  via equation (27) in order to obtain a total systematic error:

$$\sigma_{N_L(syst.)} = \sqrt{\sigma_{Fit(sys.)}^2 + \sigma_{N_L(sig.)}^2} \quad (27)$$

The statistical fit error was calculated as:

$$\sigma_{N_L(stat.)} = \frac{\sigma_{Fit(stat.)}}{E_e} \quad (28)$$

More information on the individual errors can be found in the next section.

## 4 Error Budget

This section gives an overview of all the systematic errors considered in this thesis and how they are estimated. A summary can be found in figure 69. A detailed description of what each error is can be found in the table's caption.

slice	$\sigma_{HPGe}$	$\sigma_{E_\gamma}$	$dE_e$	$\sigma_{calib}$	$\sigma_{nonlin}$	$dE_{vis}$	$\sigma_{N_L(sig.)}$	$\sigma_{Fit}$
20°, 120-150 keV	0.005	0.153	<i>0.153</i>	0.387	1.118	<i>1.183</i>	<b>0.919</b>	<b>0.279</b>
20°, 150-180 keV	0.006	0.125	<i>0.125</i>	0.387	1.118	<i>1.183</i>	<b>0.928</b>	<b>0.279</b>
20°, 180-195 keV	0.006	0.110	<i>0.110</i>	0.387	1.118	<i>1.183</i>	<b>0.938</b>	<b>0.279</b>
20°, 195-215 keV	0.006	0.100	<i>0.100</i>	0.387	1.118	<i>1.183</i>	<b>0.954</b>	<b>0.279</b>
25°, 215-235 keV	0.005	0.092	<i>0.092</i>	0.417	1.118	<i>1.193</i>	<b>0.980</b>	<b>0.431</b>
25°, 235-255 keV	0.005	0.084	<i>0.084</i>	0.417	1.118	<i>1.193</i>	<b>0.994</b>	<b>0.431</b>
25°, 255-275 keV	0.005	0.078	<i>0.078</i>	0.417	1.118	<i>1.193</i>	<b>1.006</b>	<b>0.431</b>
30°, 275-305 keV	0.006	0.071	<i>0.071</i>	0.504	1.118	<i>1.227</i>	<b>1.039</b>	<b>0.227</b>
30°, 300-330 keV	0.007	0.065	<i>0.065</i>	0.504	1.118	<i>1.227</i>	<b>1.048</b>	<b>0.227</b>
30°, 330-360 keV	0.007	0.060	<i>0.060</i>	0.504	1.118	<i>1.227</i>	<b>1.055</b>	<b>0.227</b>
35°, 360-390 keV	0.006	0.055	<i>0.055</i>	0.455	1.118	<i>1.207</i>	<b>1.054</b>	<b>0.297</b>
35°, 390-420 keV	0.006	0.051	<i>0.051</i>	0.455	1.118	<i>1.207</i>	<b>1.060</b>	<b>0.297</b>
35°, 420-450 keV	0.006	0.047	<i>0.047</i>	0.455	1.118	<i>1.207</i>	<b>1.070</b>	<b>0.297</b>
40°, 450-480 keV	0.007	0.044	<i>0.044</i>	0.334	1.118	<i>1.167</i>	<b>1.035</b>	<b>0.023</b>
40°, 480-510 keV	0.007	0.042	<i>0.042</i>	0.334	1.118	<i>1.167</i>	<b>1.042</b>	<b>0.023</b>
40°, 510-540 keV	0.007	0.039	<i>0.039</i>	0.334	1.118	<i>1.167</i>	<b>1.051</b>	<b>0.023</b>
45°, 540-570 keV	0.007	0.037	<i>0.037</i>	0.379	1.118	<i>1.181</i>	<b>1.059</b>	<b>0.099</b>
45°, 570-600 keV	0.007	0.035	<i>0.035</i>	0.379	1.118	<i>1.181</i>	<b>1.070</b>	<b>0.099</b>
50°, 600-630 keV	0.007	0.033	<i>0.033</i>	0.429	1.118	<i>1.198</i>	<b>1.092</b>	<b>0.136</b>
50°, 630-660 keV	0.007	0.032	<i>0.032</i>	0.429	1.118	<i>1.198</i>	<b>1.095</b>	<b>0.136</b>
50°, 660-690 keV	0.008	0.031	<i>0.031</i>	0.429	1.118	<i>1.198</i>	<b>1.105</b>	<b>0.136</b>
60°, 730-760 keV	0.017	0.028	<i>0.028</i>	0.389	1.118	<i>1.184</i>	<b>1.092</b>	<b>0.141</b>
60°, 760-790 keV	0.018	0.027	<i>0.027</i>	0.389	1.118	<i>1.184</i>	<b>1.098</b>	<b>0.141</b>
70°, 820-850 keV	0.017	0.025	<i>0.025</i>	0.402	1.118	<i>1.188</i>	<b>1.105</b>	<b>0.066</b>
80°, 880-910 keV	0.020	0.023	<i>0.023</i>	0.449	1.118	<i>1.205</i>	<b>1.123</b>	<b>0.077</b>
80°, 910-930 keV	0.021	0.022	<i>0.022</i>	0.449	1.118	<i>1.205</i>	<b>1.121</b>	<b>0.077</b>
90°, 930-960 keV	0.018	0.022	<i>0.022</i>	0.419	1.118	<i>1.194</i>	<b>1.114</b>	<b>0.343</b>
90°, 960-990 keV	0.019	0.021	<i>0.021</i>	0.419	1.118	<i>1.194</i>	<b>1.115</b>	<b>0.343</b>
100°, 990-1020 keV	0.015	0.020	<i>0.020</i>	0.449	1.118	<i>1.205</i>	<b>1.123</b>	<b>0.216</b>
110°, 1020-1050 keV	0.007	0.020	<i>0.020</i>	0.419	1.118	<i>1.194</i>	<b>1.114</b>	<b>0.156</b>
120°, 1050-1080 keV	0.005	0.019	<i>0.019</i>	0.415	1.118	<i>1.193</i>	<b>1.118</b>	<b>0.257</b>

Figure 69: List of the systematic errors in percent of the total signal determined for each slice. The total systematic error of the electron's energy measurement  $dE_e = \sqrt{\sigma_{HPGe}^2 + \sigma_{E_\gamma}^2}$  sums the error caused by gamma energy loss (described in section 4.1) and HPGe error  $\sigma_{HPGe}$  (described in section 3.2.2).  $dE_{vis} = \sqrt{\sigma_{calib}^2 + \sigma_{nonlin}^2}$  is the total systematic error of the light measurement, which accounts for the calibration error  $\sigma_{calib}$  (described in section 4.2) and the total nonlinearity of the detector system  $\sigma_{nonlin}$  (PMTs + digitizer card).  $\sigma_{N_L(sig.)}$  is the propagated error of both  $dE_e$  and  $dE_{vis}$ .  $\sigma_{Fit}$  is the fitting bias caused by the second low energy peak and multiple scattering events (described in section 4.4)

## 4.1 Gamma Energy Loss

The two major interaction possibilities for a gamma traveling from the radioactive source to the LS are the collimator, and the wrapping plus the wall of the source cell. The most common interaction inside the collimators, in which the gamma can still escape and does not get absorbed, is small angle scattering. The same interaction takes place in the acrylic and wrapping of the source container but the chance for the gamma to get completely absorbed is close to zero. Nevertheless, the gamma loses energy in both cases. The severity was estimated by Geant4 simulations in which the energy deposited by the gammas in the collimators and source container (disregarding the wrapping) was measured. The averaged results are energy losses of 0.18 keV for the collimator and 0.026 keV for the target cell's wall. The total bias in gamma energy resulting from energy loss was therefore estimated to be 0.206 keV for all angles. The error of the HPGe detector calibration  $\sigma_{HPGe}$  together with the gamma energy loss  $\sigma_{E_\gamma}$  gives the total error for the electron energy  $dE_e$ , as shown in percentages in figure 69.

## 4.2 Accuracy of PMT Calibration

The PMT calibration described in section 3.2.4 is done by splitting each PMT's single events in a data file into intervals holding  $10^5$  events. All the intervals are then compared to a reference interval with a Kolmogorow-Smirnow test while the PMT single events in the interval are scaled with different scaling factors. The scaling factor that leads to the highest agreement of the interval to the reference interval was then at a later stage used to scale the data relative to the reference. The measure that is used to find the best agreement is called the p-value. The p-value has its highest value 1 if the two distributions are completely identical and decreases for distributions that show fewer similarities. The p-value can also be used to determine the precision of the PMT calibration. Varying the scaling factor from its optimal value decreases the p-value.

A  $\sim 60\%$  decrease of the p-value is about an  $1\sigma$  uncertainty in the scaling factor. Comparing the scaling factor at the  $\sim 60\%$ -decreased p-value to the optimal scaling factor gives the  $1\sigma$  uncertainty for that interval. The same procedure is completed for each interval, while the uncertainties are saved. To get one error representative for the whole data taking period, a RMS of the uncertainties for each PMT is calculated resulting in the individual calibration error for each waveform  $\epsilon_0^i$  and  $\epsilon_2^i$ . The same method is used later to find the calibration error for each waveform when calibrated against a reference file. In the latter calibration, the PMT single events are not divided into intervals, but rather all PMT single events of a waveform are shifted and compared to all PMT single events of the reference file, leading to two more errors  $\epsilon_0^c$  and  $\epsilon_2^c$ . To get a total PMT calibration error for a file that holds the sum of the two PMT signals, the errors are added as follows:

$$\sigma_{PMT,calib} = \sqrt{(\epsilon_0^i)^2 + (\epsilon_0^c)^2 + (\epsilon_2^i)^2 + (\epsilon_2^c)^2} \quad (29)$$

The errors of the calibration are in general less than 1%. The exact values for each data file are listed in table 69.

## 4.3 Nonlinearity of the PMT System

The PMT system consists of two PMTs and the digitizer. Both components were tested for their linearity separately. The linearity of the ET9330 tubes used in the experiment was measured relative to the well known Hamamatsu R5912 tubes deployed in the Daya Bay experiment. To measure the nonlinearity, both tubes were mounted in a light-tight box together with a LED. The output amplitudes were then compared as a function of the LED intensity. The R5912 was

operated at 1100V and the ET9330 at 1700V. At these voltages, the ratio of the output amplitudes ET9330/R5912 was about 0.64. Figure 70 shows that the measured ratios are linear to  $<1\%$  for 100 mV - 600 mV signal amplitudes. In the actual experiment, the range of amplitudes was much smaller. A previous measurement with the same method proved the tubes to be linear to  $<0.5\%$  for the range of amplitudes measured in the experiment.

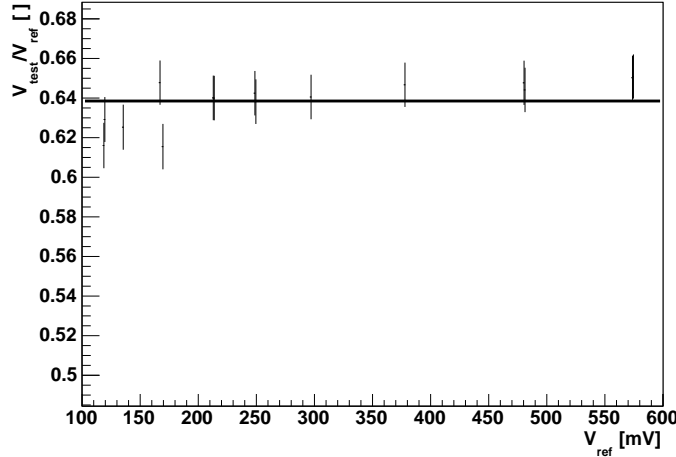


Figure 70: Ratio of ET9330/R5912 output amplitudes as a function of R5912 output amplitude

The nonlinearity of the digitizer was tested by injecting differently attenuated pulses into the digitizer and comparing them to the expected output. A Hewlett Packard pulse generator was used to generate -500 mV 20 ns wide pulses at  $\sim 100$  Hz. The pulses were then attenuated with different attenuators to match various sizes of the 'true' PMT signal over its whole range. For this purpose, a set of attenuators was used in all combinations to rule out any miscalibrated ones. In total, 14 runs at 6 different signal sizes were made. The file collected without attenuation was then used as a reference to calculate the expected signal sizes for the attenuated ones. The results collected at 3, 6, 9, 12 dB were then compared to the expected signals. There was a  $\sim 1\%$  fluctuation for repeated runs, which is believed to be a digitizer artifact. Including that artifact, the signal is within 1.328 % of the expected one. This relatively high value was used for the digitizer nonlinearity uncertainty.

#### 4.4 Bias of Fitting Procedure

The impacts of the second low energy peak and of multiple scattering were probed with Monte Carlo simulations. In this process, MC data for each angle was acquired with Geant4. Instead of slicing one coincidence region into multiple little pieces, as in the analysis, the error per angle position was determined with one projection over the whole coincidence region. An unscaled comparison between data from the experiment and MC data for the  $50^\circ$  position is illustrated in figure 71 and 72.

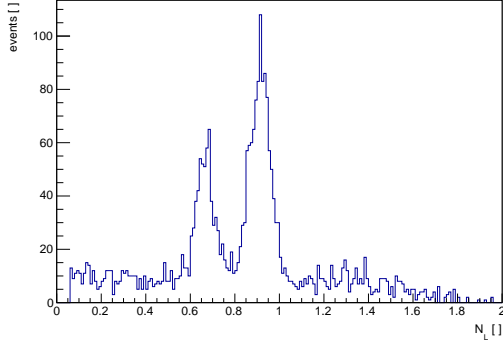


Figure 71: 600 - 660 keV projection, experimental data

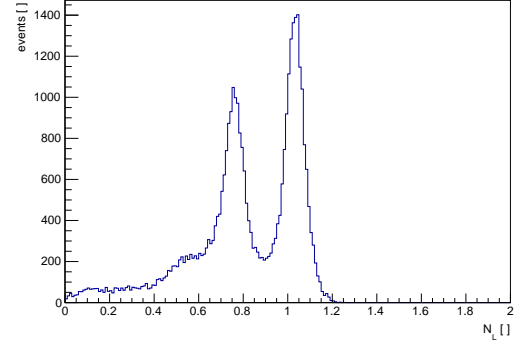


Figure 72: 600 - 660 keV projection, MC data

The MC data in figure 72 has higher statistics and no background events to the right of the 1332.5 keV peak. However, these random background events are distributed evenly over the coincidence data and do not bias the fit. Another difference between the data and MC plot is the number of multiple scattering events. In the MC data, the effect of multiple scattering seems exaggerated, but it is not when compared to a higher statistics plot of data.

To estimate the systematic error caused by fitting all angles with a simple Gaussian, MC data was used to compare the peak positions of 'golden events' to those of all events. 'Golden events' are events which only have one interaction in the LS before the gamma is fully absorbed in the HPGe detector.

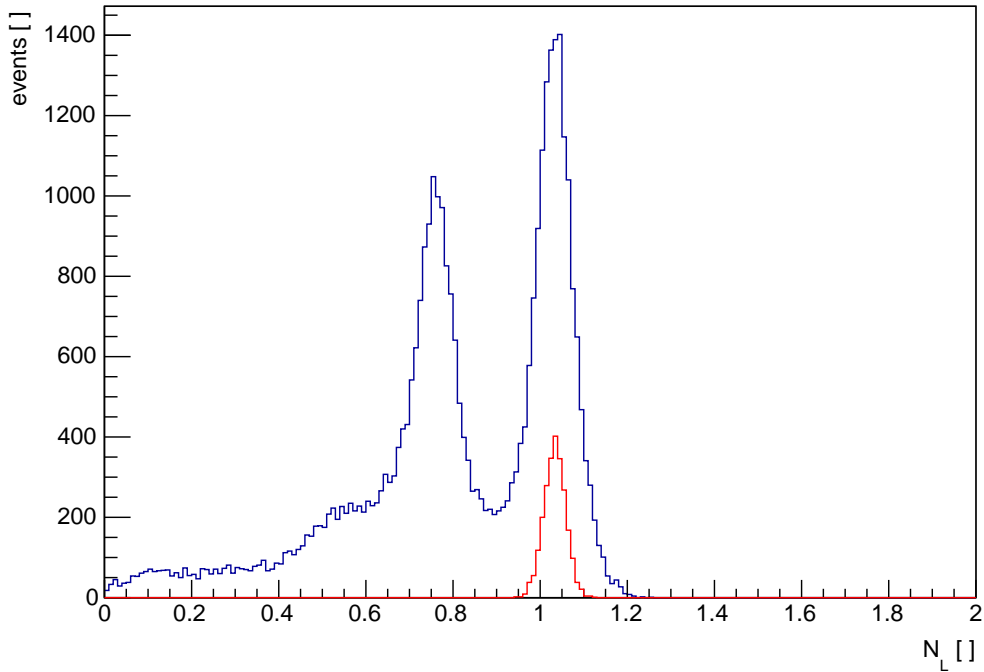


Figure 73: All data and biased peak in blue, unbiased 'golden events' in red.

Figure 73 shows all events in blue and 'golden events' in red. Since golden events are not biased in any way, the error can be estimated as the difference in peak positions. The so-obtained errors

were below 0.5 % for all angles and are listed in table 69.

## 4.5 Other Effects

Some effects are not quantitatively assessible and are therefore not included in figure 69. This section gives an overview of the possible effects and which countermeasures were taken:

**Oxygen and/or dust in the liquid scintillator:** Before the acrylic cell was assembled, all parts were cleaned two times with Alconox (an industrial cleaner known for its chemical compatibility with the Daya Bay scintillator) and deionized water (16 M $\Omega$ /cm). After the parts seemed clean, they were flushed three times with deionized water. Between each step they were dried with air. There was no visible dust particle in the cell after filling. Another concern that might affect the properties of the scintillator is oxygen that is captured during filling and storage. The liquid scintillator was stored in an air-proof glass bottle with a sealed cap. During filling there was always a laminar flow, with no 'dropping' or other disturbance. A good way to clean the LS would have been to flush it with highly clean nitrogen; this however was not done.

**Inhomogeneity in the PMT:** One location inside a photomultiplier tube might be more sensitive than another. If the light inside the target cell is slightly directional (although LS emissions should be isotropic), this could have an effect. To test the impact, a measurement was set up where the same settings were measured twice, one time with the PMT unrotated and the other time with the PMT rotated by 90°. No difference was measured.

**Cherenkov light emission:** The Cherenkov light threshold for electrons inside the LS is about 200 keV. The scintillator itself is opaque for Cherenkov light that might have been produced at these energies; however, through absorption and re-emission of Cherenkov photons by the LS, it could contribute to the nonlinearity, which then in turn would be measurable.

## 5 Summary and Results

The nonlinearity in light emission by Gd-doped linear-alkylbenzene-based scintillator in response to electrons was measured. The scintillator was excited with energetic electrons produced via Compton scattering. For this purpose, a Compton spectrometer was built which allowed variation of the scattering angle of 1332.5 MeV  $\gamma$ -rays coming from a 2.59Mbq  $^{60}\text{Co}$  source in  $5^\circ$  steps from  $20^\circ$  to  $120^\circ$ . The different scattering angles resulted in different kinetic energies of the scattered electrons, ranging from  $\sim 0.2$  to  $\sim 1.0$  MeV. The experiment was complemented by Geant4 simulations which were used to optimize the Compton spectrometer and estimate systematic errors. The result of the measurement is shown in table 74 and visualized in figure 75.

Slice	$E_e$ [keV]	$N_L$ [ ]	$\sigma_{N_L}(stat.)$ [%]	$\sigma_{N_L}(sys.)$ [%]
$20^\circ$ , 120-150 keV	$135.0 \pm 15.0$	0.773	0.525	0.961
$20^\circ$ , 150-180 keV	$165.0 \pm 15.0$	0.783	0.422	0.969
$20^\circ$ , 180-195 keV	$187.5 \pm 7.5$	0.792	0.546	0.979
$20^\circ$ , 195-215 keV	$205.0 \pm 10.0$	0.806	0.588	0.994
$25^\circ$ , 215-235 keV	$225.0 \pm 10.0$	0.821	0.601	1.071
$25^\circ$ , 235-255 keV	$245.0 \pm 10.0$	0.833	0.556	1.084
$25^\circ$ , 255-275 keV	$265.0 \pm 10.0$	0.843	0.487	1.095
$30^\circ$ , 275-305 keV	$290.0 \pm 15.0$	0.847	0.422	1.063
$30^\circ$ , 300-330 keV	$315.0 \pm 15.0$	0.854	0.313	1.072
$30^\circ$ , 330-360 keV	$345.0 \pm 15.0$	0.860	0.360	1.079
$35^\circ$ , 360-390 keV	$375.0 \pm 15.0$	0.873	0.328	1.095
$35^\circ$ , 390-420 keV	$405.0 \pm 15.0$	0.878	0.272	1.100
$35^\circ$ , 420-450 keV	$435.0 \pm 15.0$	0.886	0.262	1.110
$40^\circ$ , 450-480 keV	$465.0 \pm 15.0$	0.887	0.280	1.035
$40^\circ$ , 480-510 keV	$495.0 \pm 15.0$	0.893	0.236	1.042
$40^\circ$ , 510-540 keV	$525.0 \pm 15.0$	0.901	0.284	1.051
$45^\circ$ , 540-570 keV	$555.0 \pm 15.0$	0.897	0.254	1.063
$45^\circ$ , 570-600 keV	$585.0 \pm 15.0$	0.907	0.259	1.075
$50^\circ$ , 600-630 keV	$615.0 \pm 15.0$	0.912	0.267	1.101
$50^\circ$ , 630-660 keV	$645.0 \pm 15.0$	0.914	0.270	1.103
$50^\circ$ , 660-690 keV	$675.0 \pm 15.0$	0.923	0.309	1.114
$60^\circ$ , 730-760 keV	$745.0 \pm 15.0$	0.923	0.327	1.102
$60^\circ$ , 760-790 keV	$775.0 \pm 15.0$	0.927	0.324	1.107
$70^\circ$ , 820-850 keV	$835.0 \pm 15.0$	0.930	0.179	1.107
$80^\circ$ , 880-910 keV	$895.0 \pm 15.0$	0.932	0.194	1.126
$80^\circ$ , 910-930 keV	$920.0 \pm 10.0$	0.931	0.190	1.124
$90^\circ$ , 930-960 keV	$945.0 \pm 15.0$	0.933	0.154	1.165
$90^\circ$ , 960-990 keV	$975.0 \pm 15.0$	0.934	0.132	1.167
$100^\circ$ , 990-1020 keV	$1005.0 \pm 15.0$	0.932	0.145	1.144
$110^\circ$ , 1020-1050 keV	$1035.0 \pm 15.0$	0.933	0.086	1.125
$120^\circ$ , 1050-1080 keV	$1065.0 \pm 15.0$	0.938	0.176	1.147

Figure 74: Final results of the analysis. The plus/minus appendix of the electron energy  $E_e$  denotes the size of the slice that was projected.  $N_L$  is the extracted nonlinearity,  $\sigma_{N_L}(stat.)$  the statistical and  $\sigma_{N_L}(sys.)$  the propagated systematical error.

## Scintillator non-linearity

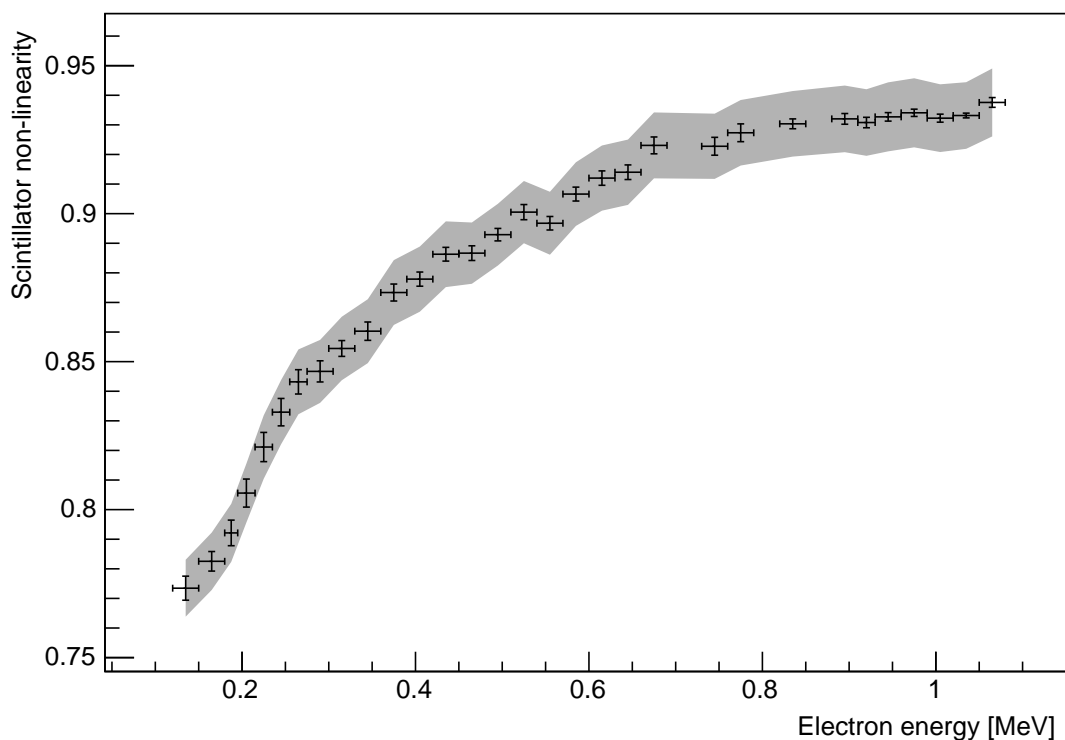


Figure 75: Measured nonlinearity; the data that was used for this plot is listed in table 74.

Looking back on the experiment, a few things could have been done better. First, the use of a 12 bit digitizer instead of an 8 bit one would have minimized the observed channel hopping. The turntable could have been rotated automatically, and instead of the  $^{60}\text{Co}$  source, which has two peaks and made fitting hard, a source with a single  $\gamma$ -decay could have been used. To decrease data taking times, multiple HPGe detectors could have been used, provided enough had been available. On the data taking side, temperature, moisture, and high voltage status of the tubes could have been continuously recorded to spot any trends.

Other than that the experiment was highly successful. The measured nonlinearity is about two times higher than the one currently used in the Daya Bay's data analysis.

## References

- [1] *Neutrino 2014 XXVI International Conference on Neutrino Physics and Astrophysics (June 2-7, 2014, Boston, U.S.A.)*.
- [2] Y. Abe et al. Background-independent measurement of  $\theta_{13}$  in Double Chooz. 2014.
- [3] J.K. Ahn et al. Observation of Reactor Electron Antineutrino Disappearance in the RENO Experiment. *Phys.Rev.Lett.*, 108:191802, 2012.
- [4] F.P. An et al. Spectral measurement of electron antineutrino oscillation amplitude and frequency at Daya Bay. *Phys.Rev.Lett.*, 112:061801, 2014.
- [5] M. Apollonio et al. Search for neutrino oscillations on a long baseline at the CHOOZ nuclear power station. *Eur.Phys.J.*, C27:331–374, 2003.
- [6] Wanda Beriguete, Jun Cao, Yayun Ding, Sunej Hans, Karsten M. Heeger, et al. Production of Gadolinium-loaded Liquid Scintillator for the Daya Bay Reactor Neutrino Experiment. 2014.
- [7] F. Boehm, J. Busenitz, B. Cook, G. Gratta, H. Henrikson, et al. Final results from the Palo Verde neutrino oscillation experiment. *Phys.Rev.*, D64:112001, 2001.
- [8] C. L Cowan Jr., F. Reines, F. B. Harrison, H. W. Kruse, A. D McGuire. Detection of the Free Neutrino: a Confirmation. *Science*, VOL. 124, NO. 3212, July.
- [9] Wikimedia Commons. Benzene representations, 2009.
- [10] J.M. Conrad. Neutrino Experiments. pages 177–254, 2007.
- [11] G. Danby, J.M. Gaillard, Konstantin A. Goulianos, L.M. Lederman, Nari B. Mistry, et al. Observation of High-Energy Neutrino Reactions and the Existence of Two Kinds of Neutrinos. *Phys.Rev.Lett.*, 9:36–44, 1962.
- [12] R. Davis. Solar neutrinos. II: Experimental. *Phys.Rev.Lett.*, 12:303–305, 1964.
- [13] D.V. Forero, M. Tortola, and J.W.F. Valle. Neutrino oscillations refitted. 2014.
- [14] S.L. Glashow. Partial Symmetries of Weak Interactions. *Nucl.Phys.*, 22:579–588, 1961.
- [15] M.C. Gonzalez-Garcia, Michele Maltoni, and Thomas Schwetz. Updated fit to three neutrino mixing: status of leptonic CP violation. 2014.
- [16] Paul Christian Hackspacher. Studies of light quenching effects in liquid scintillators and parameter determination of the buffer and veto fluids of the double chooz near detector. Master’s thesis, TU Munich, October 2014.
- [17] W.C. Haxton. The solar neutrino problem. *Ann.Rev.Astron.Astrophys.*, 33:459–503, 1995.
- [18] K. Kodama et al. Observation of tau neutrino interactions. *Phys.Lett.*, B504:218–224, 2001.
- [19] M.F. L’Annunziata. *Handbook of Radioactivity Analysis*. Elsevier Science, 2012.
- [20] Timo Lewke. *Studies of Scintillator Optical Properties, Electronics Simulation and Data Analysis for the BOREXINO Neutrino Experiment*. PhD thesis, TU Munich, October 2013.
- [21] Z. Maki, M. Nakagawa, and S. Sakata. Remarks on the unified model of elementary particles. *Prog. Theor. Phys.*, 28:870, 1962.

- [22] L.A. Mikaelyan and V.V. Sinev. Neutrino oscillations at reactors: What next? *Phys.Atom.Nucl.*, 63:1002–1006, 2000.
- [23] M. Perl, G. Abrams, A. Boyarski, M. Breidenbach, D. Briggs, F. Bulos, W. Chinowsky, J. Dakin, G. Feldman, C. Friedberg, D. Fryberger, G. Goldhaber, G. Hanson, F. Heile, B. Jean-Marie, J. Kadyk, R. Larsen, A. Litke, D. Lüke, B. Lulu, V. Lüth, D. Lyon, C. Morehouse, J. Paterson, F. Pierre, T. Pun, P. Rapidis, B. Richter, B. Sadoulet, R. Schwitters, W. Tanenbaum, G. Trilling, F. Vannucci, J. Whitaker, F. Winkelmann, and J. Wiss. Evidence for anomalous lepton production in  $e^+ - e^-$  annihilation. *Phys. Rev. Lett.*, 35:1489–1492, Dec 1975.
- [24] Abdus Salam. Weak and electromagnetic interactions. In Nils Svartholm, editor, *Elementary particle theory*, pages 367–377. Almquist & Wiksell.
- [25] J. D. Valentine and B. D. Rooney. Design of a Compton spectrometer experiment for studying non-linearity and intrinsic energy resolution. *Nucl.Instrum.Meth.*, A353:37–40, 1994.
- [26] H. Wan Chan Tseung, J. Kaspar, and N. Tolich. Measurement of the dependence of the light yields of linear alkylbenzene-based and EJ-301 scintillators on electron energy. *Nucl.Instrum.Meth.*, A654:318–323, 2011.
- [27] Steven Weinberg. A Model of Leptons. *Phys.Rev.Lett.*, 19:1264–1266, 1967.
- [28] Michael Wilking. New Results from the T2K Experiment: Observation of  $\nu_e$  Appearance in a  $\nu_\mu$  Beam. *PoS*, EPS-HEP2013:536, 2013.
- [29] Woon-Seng Choong, Member, IEEE, Giulia Hull, William W. Moses, Fellow, IEEE, Kai M. Vetter, Stephen A. Payne, Nerine J. Cherepy, and John D. Valentine, Senior Member, IEEE. Performance of a Facility for Measuring Scintillator Non-Proportionality. *IEEE TRANSACTIONS ON NUCLEAR SCIENCE*, VOL. 55, NO.3, JUNE 2008.
- [30] Fei-Hong Zhang, Bo-Xiang Yu, Wei Hu, Ma-Sheng Yang, Guo-Fu Cao, et al. Measurement of the liquid scintillator nonlinear energy response to electron. 2014.